SMG6-dependent nonsense-mediated decay maintains dsRNA homeostasis and suppresses immunogenic transcripts in a hepatocellular carcinoma model

Enes S. Arpa [1], Virginie Ricci [1], Ilja E. Shapiro [2], Marija Jokic [3], Yahya Mohammadzadeh [4], Lisa Bertrand [1], Irene Gonzalez-Menendez [5,6], Leticia Quintanilla-Martinez [5,6], Alexandre P. Bénéchet [7], Jan Rehwinkel [8], Tatiana V. Petrova [4], Sanjiv A. Luther [3], Michal Bassani-Sternberg [2], David Gatfield [1,*]

[1] Center for Integrative Genomics, University of Lausanne, Lausanne, Switzerland.
[2] Ludwig Institute for Cancer Research, University of Lausanne, Lausanne, Switzerland; Department of Oncology, Centre Hospitalier Universitaire Vaudois (CHUV), Lausanne, Switzerland; Agora Cancer Research Centre, 1011 Lausanne, Switzerland.
[3] Department of Immunobiology, University of Lausanne, Epalinges, Switzerland.
[4] Department of Oncology, Ludwig Institute for Cancer Research Lausanne and University of Lausanne, Lausanne, Switzerland.
[5] Department of Pathology and Neuropathology, University Hospital Tübingen, University of Tübingen, Tübingen, Germany.
[6] Cluster of Excellence iFIT (EXC 2180) “Image-Guided and Functionally Instructed Tumor Therapies”, Eberhard-Karls University of Tübingen, Tübingen, Germany.
[7] In Vivo Imaging Facility (IVIF), Department of Research and Training, Lausanne University Hospital and University of Lausanne, Lausanne, Switzerland.
[8] Medical Research Council Translational Immune Discovery Unit, Medical Research Council Weatherall Institute of Molecular Medicine, Radcliffe Department of Medicine, University of Oxford, Oxford, UK.
[*] Correspondence: david.gatfield@unil.ch

Abstract

The nonsense-mediated mRNA decay (NMD) pathway degrades transcripts bearing premature termination codons (PTCs), typically arising from mutations and RNA processing errors, to prevent the accumulation of aberrant proteins. Its role in cancer is complex, with both tumor-promoting and tumor-suppressive functions described. Here, we selectively inhibit NMD in the liver by conditionally inactivating its endonuclease SMG6 in a genetic mouse model of hepatocellular carcinoma. SMG6 inactivation completely abrogates tumor formation and elicits both innate and adaptive immune responses. Mechanistically, SMG6 deficiency activates the type I interferon response via the double-stranded RNA (dsRNA) sensor MDA5, uncovering a physiological role for NMD in regulating cytoplasmic dsRNA levels. In parallel, stabilization and translation of NMD-target transcripts generate non-canonical immunopeptides presented by MHC-I, promoting potent $CD8^+$ T-cell responses. These findings establish SMG6-dependent NMD as a core orchestrator of immune tolerance in cancer and reveal that its selective

inhibition in cancer cells unleashes immunogenic transcript expression with therapeutic potential.

Introduction

Eukaryotic cells employ nonsense-mediated mRNA decay (NMD) as a critical post-transcriptional quality control mechanism that degrades transcripts harboring premature termination codons (PTCs), thereby preventing the accumulation of truncated, potentially toxic proteins [1, 2]. PTCs typically arise from mutations, transcriptional errors, or splicing defects. In addition to its canonical surveillance function, NMD is increasingly recognized as a broad regulator of gene expression, shaping the transcriptome through selective degradation of physiological mRNAs [3]. NMD is executed by a multiprotein machinery centered on the helicase UPF1, and elicits mRNA cleavage through the endonuclease SMG6, followed by further exonucleolytic degradation [2].

In cancer, the role of NMD is multifaceted and context-dependent [4]. On the one hand, it may suppress tumorigenesis by limiting the expression of mutated, potentially oncogenic transcripts. On the other, it can promote immune evasion by eliminating mRNAs that encode neoantigens, particularly those arising from frameshift-inducing insertion/deletion (indel) mutations that are common in cancer genomes. By suppressing such immunogenic RNAs, NMD may dampen anti-tumor immune surveillance and reduce responsiveness to immunotherapies [5-9].

Previous studies investigating NMD in cancer have primarily relied on global depletion of core NMD components such as UPF1 or SMG proteins in cell lines or transplantable tumor models [10-14]. These approaches are limited in their ability to capture early tumorigenic events and the dynamics of immune surveillance. Moreover, these models often conflate NMD-specific effects with pleiotropic roles of UPF/SMG proteins in genome stability, telomere maintenance, and other essential processes [15].

To address these limitations, we developed a liver-specific, inducible mouse model that selectively disables the endonuclease activity of SMG6 without ablating the protein entirely [16]. We combined this model with a genetic background of hepatocellular carcinoma (HCC) driven by hepatic deletion of *Pten* and *Tsc1*, which closely mirrors human disease progression [17]. Using this physiologically relevant system, we demonstrate that selective inactivation of SMG6 triggers robust innate and adaptive immune responses and potently suppresses liver tumorigenesis. Mechanistically, for the innate immune response, we uncover that SMG6 loss induces a type I interferon (IFN) response via activation of the cytosolic double-stranded RNA (dsRNA) sensor MDA5. This reveals an unexpected physiological role for NMD in maintaining

71 cytoplasmic dsRNA homeostasis and preventing aberrant activation of antiviral immunity. In
72 validation of the long-standing neoantigen hypothesis, we find that the adaptive immune
73 response is driven by the stabilization and translation of NMD-targeted transcripts, which give
74 rise to non-canonical peptides presented on MHC-I and elicit infiltration by $CD8^+$ T-cells.
75 Together, our findings establish SMG6-dependent NMD as a central regulator of immune
76 tolerance in the liver and highlight its selective inhibition as a promising strategy to promote
77 immunogenicity in cancer.

78 **Results**

79 **HCC suppression through mutant SMG6**

80 We recently developed a conditional NMD loss-of-function mouse model that specifically
81 targets the endonucleolytic activity of SMG6 (**Extended Data Fig. 1a)** [16]. This is achieved
82 through Cre/loxP-mediated conversion of a wild-type protein-expressing *Smg6*^{flox} allele to
83 *Smg6*^{mut}, in which point mutations inactivate the catalytic residues of the PIN (PilT N-terminus)
84 nuclease domain. This approach overcomes the limitations of full NMD factor knockouts, which
85 often impair general cellular fitness due to both NMD-dependent and -independent functions
86 of these proteins [15, 18]. Liver-specific *Smg6*^{mut} mice (i.e., *Smg6*$^{flox/flox}$; *Alb*^{CreERT2} animals treated
87 with tamoxifen to activate CreERT2 in hepatocytes) display overall mild phenotypes [16],
88 underscoring the model's suitability for probing NMD function *in vivo*, including in disease-
89 relevant contexts.
90 To investigate the consequences of SMG6 inactivation on tumorigenesis, we combined this
91 NMD allele with a genetic model of hepatocellular carcinoma (HCC). This model (**Fig. 1a**)
92 employs conditional knockout alleles of the tumor suppressors *Pten* and *Tsc1*, which encode
93 inhibitors of the mTOR pathway. Liver-specific knockout of these genes (hereafter referred to
94 as L-dKO) promotes lipogenesis and drives the progression from non-alcoholic fatty liver
95 disease (NAFLD) at early stages, to non-alcoholic steatohepatitis (NASH) and, ultimately, HCC
96 at late stages [17], closely recapitulating disease evolution in humans [19].
97 We first assessed the impact of *Smg6*^{mut} on HCC formation and progression at late stages, i.e.
98 beginning from week 12 post-tamoxifen (**Fig. 1a**). Weekly magnetic resonance imaging (MRI)
99 revealed liver tumors in L-dKO *Smg6*^{wt} mice (**Fig. 1b**), whose rapid progression necessitated
100 euthanasia by week 17 due to advanced-stage HCC (**Fig. 1c**). In contrast, L-dKO *Smg6*^{mut}
101 mice developed no tumors and none required sacrifice, indicating complete suppression of the
102 HCC phenotype (**Fig. 1c**).
103 Macroscopic and histological analyses confirmed HCC in L-dKO *Smg6*^{wt} (**Fig. 1d**, top). In L-
104 dKO *Smg6*^{mut} mice, persisting until the endpoint at week 21 post-tamoxifen, we observed
105 prominent duct proliferation and moderate perisinusoidal and periportal fibrosis (**Fig. 1d**,

106 bottom). These changes disrupted the hepatic parenchyma and resulted in a nodular tissue
107 architecture. Notably, no histological evidence of HCC was detected, and L-dKO *Smg6*^{mut} livers
108 showed elevated CD8^{+} T-cell infiltration compared to L-dKO *Smg6*^{wt} (**Fig. 1e, f**), consistent
109 with sustained adaptive immune activation. Serum markers of liver injury (ALT, AST, LDH;
110 **Extended Data Fig. 1b-d**) were similarly elevated in L-dKO *Smg6*^{mut} and L-dKO *Smg6*^{wt}
111 animals at the late stage, and both groups exhibited comparable hepatomegaly (**Extended**
112 **Data Fig. 1e**). As essential controls, L-dKO *Smg6*^{mut} livers retained expression of the
113 recombined, mutant *Smg6* mRNA (**Extended Data Fig. 1f**) and lacked PTEN and TSC1
114 proteins from hepatocytes (**Figures 1g-i**), with remaining protein localized to non-parenchymal
115 cells such as Kupffer cells (**Figure 1j**). These findings ruled out trivial explanations for the
116 absence of HCC – such as synthetic lethality of the *Smg6*^{mut}; *Pten*^{ko}; *Tsc1*^{ko} genotype and
117 regeneration by non-mutant tissue – and demonstrate that tumor suppression is specifically
118 due to the interaction between mutant SMG6 and the tumor-prone L-dKO background. In
119 summary, we concluded that inhibition of NMD via *Smg6* mutation prevents cancer formation
120 in this genetic model of HCC.

121 **SMG6 inactivation promotes early immune infiltration**

122 Given the striking phenotypic divergence at late stages – tumors in *Smg6* wild-type mice but
123 none in *Smg6* mutants – we next investigated the early stages in our genetic model, at 3 weeks
124 post-tamoxifen (**Fig. 1a**), with the aim of understanding the molecular and cellular changes
125 occurring in NMD-deficient livers prior to tumor development. As expected, Western blot
126 analysis at this early time point confirmed strong depletion of TSC1 and PTEN proteins in L-
127 dKO livers, regardless of *Smg6* genotype (**Fig. 2a, b**).
128 Macroscopic and histological analyses revealed comparable NASH features in both *Smg6*^{wt} or
129 *Smg6*^{mut} L-dKO livers, including focal microsteatosis, hepatocyte ballooning, inflammatory
130 infiltration, and necrosis (**Fig. 2c; Extended Data Fig. 2a**). However, inflammation was already
131 markedly more pronounced in L-dKO *Smg6*^{mut} livers at this early stage, as shown by increased
132 staining for the neutrophil/monocyte marker myeloperoxidase (MPO; **Fig. 2d**, left panels) and
133 the cytotoxic T-cell marker CD8 (**Fig. 2d**, right panels: **Fig. 2e**). Flow cytometry further
134 confirmed elevated hepatic leukocyte counts in L-dKO *Smg6*^{mut} livers (**Fig. 2f-h; Extended**
135 **Data Fig. 2b, c**). Consistent with this heightened inflammatory state, serum levels of liver injury
136 markers also peaked specifically in L-dKO *Smg6*^{mut} animals at this early time point (**Extended**
137 **Data Fig. 1b-d**).
138 Interestingly, increased immune cell infiltration was also observed in *Smg6*^{mut} livers lacking the
139 L-dKO alleles, indicating that NMD inhibition alone promotes a pro-inflammatory hepatic
140 environment (**Fig. 2i, j**). Notably, when *Smg6* mutation was combined with L-dKO alleles,
141 infiltration was further enhanced – particularly for innate immune populations such as

142 neutrophils and Ly6C^{high} and Ly6C^{low} monocytes (**Fig. 2g-j**). In addition, L-dKO *Smg6^{mut}* livers
143 displayed elevated apoptotic markers (**Extended Data Fig. 2d-h**) and increased expression of
144 pro-fibrotic genes (**Extended Data Fig. 2i**), consistent with heightened cell death and liver
145 injury. Together, these findings demonstrate that SMG6 inactivation potentiates early liver
146 inflammation, immune cell infiltration, and apoptosis in a tumor-prone background – at a time
147 point well before overt HCC develops in this model.

148 ***Smg6* mutation induces CD8$^+$ T-cell responses through non-canonical immunopeptide**
149 **presentation**

150 To investigate the mechanism underlying the immune-altered state in *Smg6^{mut}* livers, we first
151 focused on adaptive immune activation – particularly the infiltration of CD8$^+$ T-cells (**Fig. 2j**),
152 key effectors of anti-tumor immunity. We hypothesized that NMD inhibition enables
153 hepatocytes to present novel MHC-I-bound immunopeptides derived from stabilized NMD-
154 target transcripts.

155 To test this, we employed a multi-omics approach (**Fig. 3a**), combining transcriptomics (RNA-
156 seq, to uncover NMD-regulated transcripts), ribosome profiling (Ribo-seq, to detect translated
157 open reading frames), and immunopeptidomics (mass spectroscopy-based identification of
158 MHC-I-bound peptides). This strategy enables the identification of peptides uniquely presented
159 in *Smg6^{mut}* livers and to trace their origin to NMD-regulated transcripts.

160 Immunopeptidomics analyses identified over 2,000 MHC-I-bound peptides (**Fig. 3b**), most of
161 which were shared between *Smg6^{mut}* and *Smg6^{wt}* livers and mapped to canonical coding
162 sequences (**Fig. 3c; Supplementary Table 1**). However, 18 peptides were detected
163 exclusively in *Smg6^{mut}* livers across all replicates, compared to only 4 peptides unique to
164 *Smg6^{wt}* – a highly significant enrichment of *Smg6^{mut}*-specific peptides (P = 5.4e-05; Fisher's
165 exact test). Among these, four peptides originated from non-canonical coding regions: three
166 from exonic sequences and one from an intronic region (**Fig. 3c**, middle and right panels).

167 For example, the peptide SAPDGIKTPM mapped to the *D17H6S56E-5* gene, previously
168 annotated as a long non-coding RNA with sequence similarity to a mouse leukemia virus (MLV)
169 envelope gene [20]. RNA-seq analysis revealed elevated expression of this transcript in *Smg6^{mut}*
170 livers (**Fig. 3d**), especially for exon-mapping reads, whereas intronic read levels were only
171 modestly increased (**Fig. 3e**). Since intron-mapping reads can serve as a proxy for
172 transcriptional output [21], these data suggest that *D17H6S56E-5* upregulation is primarily post-
173 transcriptional, consistent with its identity as an NMD target. Ribo-seq further confirmed
174 translation of a 596-amino acid (aa) open reading frame (ORF) containing the SAPDGIKTPM
175 epitope near its N-terminus (**Fig. 3d**, right panel). Similarly, the VVITFSKM peptide originated
176 from the *Gm6545*/*A330040F15Rik* locus, a pseudogene copy of *Fam111a*, which showed
177 increased RNA expression and ribosome occupancy of a 554-aa ORF (**Extended Data Fig.**

178 3a). The remaining two peptides – VSTTNFTHA and AGPSNSEIHL – mapped to an out-of-
179 frame product from the *Hemojuvelin (Hjv)* locus and an intronic sequence of *Transferrin (Trf)*,
180 respectively (**Supplementary Table 1**). Together, these findings indicate that NMD inhibition
181 enables the expression and translation of non-canonical transcripts, which give rise to novel
182 MHC-I-presented peptides – potentially accounting for the observed $CD8^+$ T-cell activation.
183 To test their immunogenicity, we assessed whether the four $Smg6^{mut}$-specific non-canonical
184 peptides could activate $CD8^+$ T-cells, using leukocytes isolated from the spleen and liver of
185 $Smg6^{wt}$ and $Smg6^{mut}$ mice three weeks post-tamoxifen (**Fig. 3f**). First, we noted that the
186 NetMHCpan rank predictions indicated strong binding affinity for all four peptides (rank < 2%;
187 **Fig. 3g**). Next, we chemically synthesized the four non-canonical peptides and used them as
188 a pool to determine their immunogenic potential. To assess specificity, we compared with two
189 control pools in our assay: one with commonly detected peptides and one with $Smg6^{mut}$-
190 specific canonical peptides (**Fig. 3c, g**). Upon stimulation with the $Smg6^{mut}$-specific non-
191 canonical peptide pool, $CD8^+$ T-cells from both spleen and liver of $Smg6^{mut}$ mice showed a
192 robust increase in IFNγ expression (**Fig. 3h; Extended Data Fig. 3b, c**). In contrast, leukocytes
193 from $Smg6^{wt}$ mice showed no such response, and neither of the control peptide pools elicited
194 $IFN\gamma^+CD8^+$ T-cell activation in either genotype (**Fig. 3h**). Together, these results establish that
195 $Smg6^{mut}$-specific non-canonical peptides are processed and presented via MHC-I and can
196 elicit robust $CD8^+$ T-cell activation *in vivo*.

197 **SMG6 inactivation triggers a cell-autonomous type I IFN response**

198 We next investigated whether the observed innate immune infiltration might also stem from a
199 cell-intrinsic, SMG6-dependent mechanism. Supporting this hypothesis, RNA-seq analysis
200 revealed broad upregulation of transcripts indicative of an activated type I interferon response
201 (**Fig. 4a**) [22]. Quantitative real-time PCR (qPCR) confirmed strong $Smg6^{mut}$-dependent induction
202 of canonical IFN-stimulated genes (ISGs), including *Ifih1*, *Oas1a*, *Ifi44*, *Zbp1*, and *Ifit1* (**Fig.**
203 **4b**), consistent with robust activation of the type I IFN pathway.
204 Given that whole liver tissue contains both $Smg6^{mut}$ hepatocytes and $Smg6^{wt}$ immune cells,
205 ISG induction could result either from hepatocyte-leukocyte interactions or from a cell-
206 autonomous effect of SMG6 loss-of-function. To distinguish between these possibilities, we
207 used $Smg6^{flox/flox}$ primary tail fibroblasts transduced with tamoxifen-activatable *CreERT2* (**Fig.**
208 **4c**) [16]. Tamoxifen treatment efficiently abrogated NMD, as evidenced by >10-fold increase in
209 accumulation of an NMD-sensitive *Hnrnpl* splice variant (**Fig. 4d**). Crucially, NMD inactivation
210 triggered massive ISG upregulation, with *Ifih1*, *Oas1a*, *Ifi44*, *Zbp1*, and *Ifit1* increasing by up
211 to several hundredfold (**Fig. 4e**), establishing that loss of SMG6 activity is sufficient to induce
212 a type I IFN response in a cell-autonomous manner. To assess IFN pathway activation at the
213 protein level, we measured CXCL10, an IFN-inducible chemokine and well-established

214 surrogate for type I IFN signaling [23]. CRE-treated *Smg6*^{flox} fibroblasts displayed markedly
215 elevated CXCL10 levels compared to all relevant controls (**Fig. 4f**), further supporting
216 autonomous IFN pathway activation under *Smg6*^{mut} conditions. Importantly, all genotypes
217 responded comparably to poly I:C stimulation, reaching similarly high CXCL10 levels (**Fig. 4f**),
218 indicating that the downstream IFN signaling machinery remains intact and inducible across
219 conditions. Together, these findings demonstrate that SMG6 endonuclease inactivation drives
220 a cell-intrinsic type I IFN response, independent of immune cell interactions, in both liver tissue
221 and fibroblasts.

222 **Increased abundance of intron-retaining transcripts in *Smg6*^{mut} livers**

223 The type I IFN response is a key antiviral pathway triggered when cytoplasmic sensors detect
224 atypical nucleic acids, such as dsRNA. Although typically associated with viral infection,
225 endogenous sources of dsRNA – arising from dysregulated RNA processing – can similarly
226 enhance anti-tumor immunity or induce apoptosis. One such mechanism involves splicing
227 inhibition, which promotes leakage of intron-containing mRNAs into the cytoplasm. These
228 transcripts can form dsRNA structures, often due to repetitive element sequences embedded
229 within introns [24-26].
230 Transcripts with retained introns are well-established NMD substrates in mammals [27, 28], as
231 also shown in our previous work using *Smg6*^{mut} fibroblasts [16]. We therefore asked whether a
232 similar accumulation of intron-retaining transcripts occurs in *Smg6*^{mut} livers. Using hepatic
233 RNA-seq data, we performed differential expression analysis focusing on annotated intron-
234 retaining isoforms. This revealed a marked increase in over 500 such isoforms in *Smg6*^{mut}
235 livers, compared to only 81 showing significantly reduced abundance (**Fig. 4g**). Inspection of
236 representative gene loci confirmed that exonic read coverage – shared by canonical and intron-
237 retaining isoforms – remained largely unchanged, while intronic read coverage was markedly
238 elevated (**Fig. 4h, i**), supporting specific enrichment of intron-containing transcripts. Notably,
239 we identified introns predicted to form dsRNA structures due to the presence of oppositely
240 oriented repetitive elements. For example, the retained intron in *Phkg2-208* (**Fig. 4i**) harbors
241 two SINE/B1 elements in sense and antisense orientation, resulting in extensive
242 complementarity predicted to support intramolecular dsRNA formation (**Fig. 4j, k**). Additional
243 transcript category analyses from the RNA-seq dataset, revealing a global increase in lncRNAs
244 and NMD-targets, alongside a reduction in protein-coding isoforms, are shown in (**Extended
245 Data Fig. 4a-c**).
246 Together, these findings demonstrate that SMG6 inactivation leads to widespread
247 accumulation of intron-retaining transcripts in the liver, which may serve as endogenous
248 sources of immunostimulatory dsRNA and contribute to type I IFN activation.

249 **MDA5 is required for the SMG6-dependent type I IFN response**

250 The widespread accumulation of intron-retaining transcripts in *Smg6*^{mut} livers and fibroblasts
251 suggests a source of endogenous dsRNA capable of triggering innate immune signaling. To
252 identify how this immunogenic RNA is sensed, we focused on the cytoplasmic dsRNA
253 receptors MDA5 and RIG-I, both of which activate type I IFN responses via MAVS [29]. Since
254 RIG-I preferentially detects short dsRNAs with 5′-triphosphate ends – a hallmark of viral RNAs
255 [29] – we hypothesized that MDA5, which may recognize longer, structured dsRNA species [30],
256 mediates the response to *Smg6* inactivation.

257 To test this, we generated *Smg6*$^{flox/flox}$ fibroblast lines lacking *Ifih1*, the gene encoding MDA5
258 (**Fig. 5a**, **Extended Data Fig. 5a, b**), and induced *Smg6* mutation using recombinant, cell-
259 permeable TAT-Cre protein (**Fig. 5b**). NMD inhibition remained intact in MDA5-deficient cells,
260 as evidenced by increased accumulation of the NMD-sensitive *Hnrnpl* splice variant (**Fig. 5c**).
261 Strikingly, however, ISG induction – robust in MDA5-proficient *Smg6*^{mut} cells – was nearly
262 abolished in the absence of MDA5 (**Fig. 5d**), demonstrating that this sensor is essential for the
263 SMG6-dependent IFN response. Consistent with the accumulation of immunogenic RNA,
264 cytoplasmic dsRNA levels were significantly elevated in *Smg6*^{mut} fibroblasts, as detected by
265 increased J2 antibody staining (**Fig. 5e, f**) [31].

266 These results identify MDA5 as the critical sensor linking SMG6 inactivation to type I IFN
267 activation, via detection of endogenous dsRNA. Moreover, the specificity of this response –
268 and its absence in Cre-treated MDA5-deficient cells – rules out confounding activation of
269 alternative pathways such as cGAS-STING, previously associated with Cre-mediated DNA
270 damage [32]. Together, our findings establish SMG6-dependent NMD as a key RNA quality
271 control mechanism that prevents the accumulation of endogenous dsRNA and inappropriate
272 activation of MDA5 and type I IFN signaling — thereby preserving innate immune quiescence
273 in non-infected cells.

274 **Discussion**

275 Using a unique combination of tissue-specific NMD inactivation with a fully immunocompetent
276 genetic cancer model for HCC, we provide *in vivo* evidence that loss of the endonuclease
277 activity of SMG6 triggers both innate and adaptive immune mechanisms and potently acts to
278 prevent tumor development. Specifically, our study validates the long-standing "neoantigen
279 hypothesis", showing that aberrant transcripts normally degraded by NMD give rise to non-
280 canonical peptides presented on MHC-I and elicit CD8^{+} T-cell responses. Unexpectedly, we
281 also uncover a second, previously unrecognized regulatory function of NMD, which may
282 arguably represent the more fundamental function of the pathway: SMG6 curtails aberrant
283 innate immune activation by preventing the cytoplasmic accumulation of immunostimulatory
284 dsRNAs. These dsRNAs, which can endogenously derive from intron-retaining transcripts

285 enriched in repetitive elements, are sensed by MDA5 and trigger a type I interferon response.
286 Together, these findings establish SMG6 as a molecular gatekeeper that maintains immune
287 quiescence by eliminating immunogenic RNA species before they engage dsRNA sensing
288 pathways or are translated into novel immunopeptide-containing proteins.
289 This dual role of SMG6 significantly reframes our understanding of NMD. Traditionally viewed
290 as a translation-coupled protein quality control system, NMD has been understood primarily in
291 terms of its ability to eliminate aberrant transcripts containing premature termination codons,
292 thereby preventing the accumulation of truncated, potentially toxic proteins. Our results extend
293 this view to include an RNA-centered function: controlling the abundance of specific
294 cytoplasmic RNAs (that is, dsRNAs) to prevent background activation of immune sensors. In
295 this light, SMG6 joins other RNA-modifying or -processing factors such as ADAR1 that act to
296 silence endogenous dsRNA signals and uphold self-tolerance [33].
297 Viewed from an evolutionary perspective, this RNA-centric function may represent a key
298 selective pressure driving the conservation of the pathway. While the suppression of toxic
299 proteins remains a valid functional rationale, the more immediate threat posed by the activation
300 of innate immune sensors – such as MDA5 and PKR – by endogenous RNAs may have
301 provided strong evolutionary pressures as well. These sensors are exquisitely tuned to
302 recognize features common to viral nucleic acids but can be inadvertently activated by
303 endogenous transcripts when RNA processing or degradation fails. In this context, SMG6-
304 mediated degradation acts as a buffer, maintaining the cytoplasmic RNA environment below
305 an immunostimulatory threshold. The parallels to mechanisms implicated in autoimmune and
306 inflammatory pathologies suggest that dysregulation of NMD could contribute to a wider
307 spectrum of diseases than previously appreciated [34].
308 Finally, our study positions SMG6 as a potential therapeutic target in oncology. In our
309 immunocompetent HCC model, liver-specific inactivation of SMG6 prevents tumor
310 development through robust immune activation. This supports the concept that NMD inhibition
311 can convert immunologically "cold" tumors into "hot" ones by exposing them to both innate and
312 adaptive immune surveillance. The challenge ahead lies in achieving selective modulation:
313 while transient, tissue-restricted inhibition of SMG6 could unleash anticancer immunity, it also
314 risks triggering inflammation, as evidenced by the development of steatohepatitis and fibrosis
315 in our model. Nonetheless, our results point to the exciting possibility that pharmacological
316 inhibition of SMG6's endonuclease activity may be harnessed to therapeutically manipulate
317 the immunogenicity of cancer, provided its immune-stimulatory effects can be balanced
318 against potential toxicity.

Methods

Animals

All animal experiments were conducted in accordance with the cantonal guidelines of the Canton of Vaud, Switzerland, license VD3739. Healthy adult male mice of age 8 to 10 weeks were used. Animals with *Alb*^{CreERT2}; *Smg6*^{wt} and *Alb*^{CreERT2}; *Smg6*^{flox} alleles were maintained on a C57BL/6J background. Mice with *Alb*^{CreERT2}; *Pten*^{flox}; *Smg6*^{wt}; *Tsc1*^{flox} and *Alb*^{CreERT2}; *Pten*^{flox}; *Smg6*^{flox}; *Tsc1*^{flox} alleles were maintained on a hybrid background (C57BL/6J, 129SvJ, and BALB/2c). The alleles *Alb*^{CreERT2}, *Pten*^{flox}, *Smg6*^{flox}, and *Tsc1*^{flox} have been previously described [16, 35-37].

Induction of hepatocyte-specific *Pten* & *Tsc1* double knockout and *Smg6* mutation

8- to 10-week-old male L-dKO *Smg6*^{wt} and *Smg6*^{flox} mice, carrying the liver-specific *Albumin*-driven *CreERT2*, and their control littermates received four intraperitoneal injections of tamoxifen, dissolved in corn oil at a dosage of 75 mg/kg of body weight, in the consecutive days. The early-stage mice were euthanized 3 weeks after tamoxifen injections. In the late-stage experiment, L-dKO *Smg6*^{wt} mice were euthanized based on the progression of HCC (latest at week 17). Animals in the other groups (Ctrl *Smg6*^{wt}, Ctrl *Smg6*^{mut} and L-dKO *Smg6*^{mut}) were euthanized 21 weeks after tamoxifen injections.

Magnetic resonance imaging (MRI)

Mice were scanned weekly (starting from week 12), to monitor HCC evolution and progression, using a 3 Tesla small animal MRI scanner (Bruker BioSpin MRI, Ettlingen, Germany) with a 40-mm volume coil as a transmitter. Animals were anaesthetized using isoflurane (Attane) at 3-4% for 2 min. When fully sedated, animals were transferred into the MRI machine. The imaging procedure was performed under 1.5% isoflurane in oxygen. Data was acquired via Paravision 360 v2.0 software.

Histopathology and immunohistochemistry analyses

Livers were fixed in 4% buffered formalin for 24 h and embedded in paraffin. For histology 3-5 µm-thick sections were cut and stained with Hematoxylin and Eosin (H&E) and Masson's Trichrome (MTC). Immunohistochemistry was performed on an automated immunostainer (Ventana Medical Systems, Inc.) according to the company's protocols for open procedures with slight modifications. All slides were stained with the antibodies CD4 (SP35; Zytomed, Berlin, Germany), CD8 (C8/144B; Dako, Glostrup, Denmark), PTEN (Cell Signaling Technology, 9188), Cleaved-Caspase3 (Cell Signaling Technology, 9661), and MPO (anti-MPO Ab-1, Lab Vision UK, Ltd., Newmarket, Suffolk, Great Britain). Appropriate positive and negative controls were used to confirm the adequacy of the staining. The histologic samples

353 were analyzed by an experienced pathologist (L. Quintanilla-Martinez). All samples were
354 scanned with the Ventana DP200 (Roche, Basel, Switzerland) and processed with the Image
355 Viewer MFC Application. Final image preparation was performed with Adobe Photoshop 2024.

356 **Intrahepatic leukocyte isolation and flow cytometry staining**

357 Leukocytes in liver were isolated as described previously [38]. Mice were euthanized and
358 subsequently perfused with 10 ml 1x PBS via the inferior vena cava. 1 g of liver tissue was
359 excised from each mouse and placed into a tube containing 10 ml RPMI. The tissues were
360 then crushed using 70 µm cell strainers and a plunger, ensuring all pieces were passed through
361 the strainer. The resulting cell suspensions were centrifuged at 1600 x g for 5 min. The cell
362 pellets were resuspended in a solution containing 2 mg collagenase, 25 µl DNase and 10 ml
363 RPMI. The mixture was incubated at 37°C for 40 min, constantly stirring. After incubation, 25
364 ml RPMI was added to dilute the mixture. The samples were then centrifuged at 300 x g for 3
365 min to precipitate the connective tissue. The supernatants were transferred to new tubes and
366 centrifuged at 1600 x g for 5 min. The cell pellets were then resuspended in a Percoll density
367 gradient solution (36% Percoll [Cytiva], 4% 10x PBS, 60% RPMI) and centrifuged at 2000 x g
368 for 20 min without brake. The pellets were resuspended with 2 ml of Ammonium-Chloride-
369 Potassium (ACK) lysis buffer for 2 min to lyse remaining red blood cells. Following that, 8 ml
370 RPMI was added to the tubes, and the samples were centrifuged at 1600 x g for 5 min. The
371 purified leukocyte pellets were resuspended in 1 ml HBSS. The cells were blocked with anti-
372 CD16/32 and then washed with flow cytometry buffer (1x PBS, 2% FCS, 2mM EDTA). Next,
373 the cells were incubated with following primary antibodies for 25 min at 4°C in the dark: CD19-
374 BV605 (BD biosciences, 563148), TCRb-PE (BD biosciences, 12-5961-81), CD4-biotin
375 (homemade), CD8a (Biolegend, 100750), CD44-FITC (homemade), CD11b-FITC (Biolegend,
376 101206), CD45-PE-Cy7 (Biolegend, 10114), Ly6C-BV785 (Biolegend, 128041), Ly6G-APC-
377 Cy7 (Biolegend, 127624), CD19-PE (Immunotools, 22190194), TCRb-PE (BD biosciences, 12-
378 5961-81), MHCII-BV711 (Biolegend, 107643), CD11c-biotin (homemade), NK1.1 (BV605,
379 108753), Streptavidin (APC, 405207) and BV510-Zombie aqua (Biolegend, 423102). Following
380 washes with flow cytometry buffer, the cells were incubated with secondary antibodies for 20
381 min at 4°C in the dark. The cells were fixed with BD fixation kit (554714).

382 **Serum parameters**

383 Following the euthanasia of the animals, blood was quickly collected from the decapitated
384 body, and then transferred into a lithium-heparin (LiHep) added tube (BD microtainer) to obtain
385 serum. After 30 min to 1 h incubation at room temperature (RT), samples were centrifuged
386 (2,000 g x 10 min, RT) to separate serum. Following that, 100 µl of serum was loaded to a
387 Cobas c111 analyzer to measure the levels of following enzymes: ALT, AST and LDH.

388 ***Smg6* cDNA genotyping**

389 Total RNA was prepared as described previously [39]. For each RNA sample, the following
390 reaction was assembled: 4.5 µg RNA, 1.5 µl random hexamer (100 µg/ml), 1.5 µl 10 mM
391 dNTPs, RNase-free water to 18 µl. Samples were heated for 5 min at 65°C, and then
392 immediately put on ice. A master mix containing the following was added to each tube: 6 µl 5x
393 First-strand buffer, 3 µl 0.1 M DTT, 0.375 µl RNase inhibitor, 1.5 µl RNase-free water. After a
394 short incubation (2 min, at RT), 1.125 µl Superscript II reverse transcriptase enzyme was
395 added to each reaction. Samples were incubated 10 min at 25°C, 50 min at 42°C, 15 min at
396 70°C, respectively. *Smg6* genotyping polymerase chain reaction (PCR) was performed as
397 described previously [16]. The primer sequences – encompassing both mutant sites – are as
398 follows: forward: CCA GAT ACC AAC GGC TTC AT; reverse: TCT GGG TGG ATT GGT AGC
399 TC. Reactions were run on a 0.8% agarose gel, at 100 V for 100 minutes. Bands corresponding
400 to ~620 nt were excised, and then purified using Qiaquick Gel Extraction Kit (QIAGEN, 28704).
401 DNAs were Sanger-sequenced by Microsynth.

402 **Quantitative Reverse Transcriptase PCR**

403 Total RNA was prepared, and cDNA was synthesized as mentioned above. 10-times diluted
404 cDNA templates and a master mix containing SYBR green master mix (2x), forward and
405 reverse primers (3.0 µM) were mixed, and then a 384-well plate was prepared using the Tecan
406 Freedom EVO software. RT-PCR was performed using QuantStudio6 real-time systems.
407 Relative mRNA expression levels were obtained by normalizing each CT value (mean of three
408 technical replicates) to *Rpl13* and *Rpl27* expressions. The qPCR primer sequences can be
409 found in Supplementary Table 2.

410 **Transcriptomics analysis**

411 Total RNA was prepared as mentioned above. RNA-seq libraries were prepared from
412 individual mouse livers according to the standard protocols. Single-end sequencing (150
413 bases) was performed on NovaSeq6000 (Illumina) with a sequencing depth of 400 million
414 cDNA-mapping reads in total. Sequencing reads were trimmed for the first two low quality
415 (nucleotides) nt. Trimmed reads were then mapped using STAR [40] (v2.7.11b; --twopassMode
416 Basic --seedSearchStartLmax 50 --outSAMmultNmax 1) in a sequential manner: mouse rRNA
417 (Ensembl version 39.111), human rRNA (Ensembl version 38.111), mouse tRNA, and mouse
418 genome. Read counts per genes were obtained using summarizeOverlaps() of the R (v4.4.0)
419 library GenomicAlignments (mode = 'Union') and low read counts were excluded (≤5 counts in
420 less than three samples). Differential gene expression analysis was performed using DEseq2
421 [41].

422 **Ribosome profiling**

423 The libraries for ribosome profiling were generated as [42] with slight changes. Frozen liver
424 tissues (200 mg) from individual mice were homogenized with 5 strokes using a Teflon
425 homogenizer in 3 volumes of polysome buffer (150 mM NaCl, 20 mM Tris-HCl [pH 7.4], 5 mM
426 DTT, complete EDTA-free protease inhibitors [Roche] and 40 U/ml RNasin plus [Promega])
427 supplemented with 1% Triton X-100 and 0.5% Na deoxycholate. Liver lysates were incubated
428 on ice for 10 min and cleared by centrifugation at 10,000 g, 4°C for 10 min. Supernatants were
429 flash-frozen and stored in liquid nitrogen. For each sample, 15 OD_{260} of liver lysate was
430 digested with RNase I (Ambion) for 45 min at RT under constant shaking. RNase I-digested
431 RNA was separated on 15% urea-polyacrylamide gels to excise monosome (~30 nt) footprints.
432 From the gel slices, RNA was extracted overnight at 4°C on a rotating wheel before
433 precipitation in isopropanol for 1 h, at -20°C. RNA 3'-end repair was performed with 2 U/µl of
434 T4 PNK (Lucigen) before 2 h of adapter ligation at 25°C using T4 RNA Ligase 1 (NEB) and T4
435 RNA Ligase 2 Deletion Mutant (Lucigen) and 1 µl of a 20 µM 5'-adenylated DNA adapter.
436 Adapter removal was performed by treating individual libraries with 5'deadenylase (NEB) and
437 RecJf exonuclease (NEB) for 1 h at 30°C and 1 h at 37°C. Samples were purified and pooled
438 using Zymo Clean & Concentrator columns. Ribosomal RNA was depleted according to
439 siTools Biotech rRNA depletion kit specifications with a custom-made riboPOOL. The clean-
440 up step was performed using Zymo Clean & Concentrator columns. Further library preparation
441 steps were performed as described. The amplification of libraries was performed using i5 and
442 i7 [NexteraD502 or NexteraD503] primers. Libraries were sequenced on a NovaSeq6000
443 (Illumina).

444 **Ribosome profiling data analysis**

445 Sequencing reads were cleaned and trimmed. Briefly, adapter sequences were removed using
446 cutadapt (v3.5) [43] with the following parameters --match-read-wildcards --overlap 8 --discard-
447 untrimmed --minimum-length 30. Reads were filtered by quality using FASTX Toolkit (v0.0.14;
448 -Q33 -q 30 -p 90) and by size using an in-house Python script (length 26-35 nt). Cleaned reads
449 were then mapped using STAR (--twopassMode Basic –seedSearchStartLmax 28 –
450 outSAMmultNmax 1) [40] in a sequential manner: mouse rRNA (Ensembl version 39.111),
451 human rRNA (Ensembl version 38.111), mouse tRNA, and mouse genome. STAR was used
452 for the mapping to splice junctions, as neoantigens can be produced from both exons and
453 introns. The A-site position of mapped reads to the mouse genome was retrieved using the R
454 (v4.4.0) package ribosomeProfilingQC (v1.16.0; estimatePsite() and getPsiteCoordinate(), and
455 addition of 3 nt to recover the A-site position). The A-sites were assigned to the counting bins
456 and the A-site count per bin was retrieved. Counting bins were defined using an in-house R
457 script (main functions: makeTxDbFromGFF() from txdbmaker [v1.1.1]; exonicParts() from

458 GenomicFeatures [v1.57.0]; and reduce(), gaps(), and findOverlaps() from IRanges [v2.39.2])
459 and A-site counts were obtained using summarizeOverlaps() of GenomicAlignments (v1.41.0;
460 mode = 'Union') [44]. The low A-site counts (≤5 counts in less than three samples) were excluded
461 and the differential analysis was performed using DESeq2 (v.1.45.3). To identify putative
462 neoantigens, the median A-site counts were calculated for each condition and the bins with at
463 least one A-site count in L-dKO *Smg6*^{mut} were retained. The nucleotide sequences of each bin
464 were extracted, translated in the three reading frames, and the resulting amino acid sequences
465 were then split by stop codon, and retained if the peptide sequence lengths were ≥ 8 amino
466 acids.

467 **MHC-I antibody production**

468 MHC-I monoclonal antibodies were purified from the supernatant of HB-51 and HIB 34.1.2
469 hybridoma cells (ATCC), respectively, with Protein A-Sepharose 4B beads (Invitrogen). HB-51
470 has specificity for H2-Db and H2-Kb, HIB 34.1.2 has specificity for H2-Dd, H2-Kd, and H2-Ld.
471 Each antibody type was cross-linked separately to Protein A-Sepharose 4B beads at
472 concentrations of 5 mg of antibodies per 1 ml of bead volume. To this end, the antibodies were
473 incubated with Protein A-Sepharose 4B beads for 1 hour, at RT. Antibodies and beads were
474 cross-linked with dimethyl pimelimidate dihydrochloride (Sigma-Aldrich) in 0.2 M sodium
475 borate buffer pH 9 (Sigma-Aldrich) to achieve a final concentration of 20 mM for 30 min. The
476 reaction was quenched via incubation with 0.2 M ethanolamine pH 8 (Sigma-Aldrich) for 2
477 hours. Cross-linked antibodies were stored at 4°C.

478 **Purification of MHC-I-eluted peptides**

479 200 mg of liver tissue per biological replicate was lysed in 2 ml phosphate buffered saline with
480 0.5% sodium deoxycholate (Sigma-Aldrich), 0.2 mM iodoacetamide (Sigma-Aldrich), 1 mM
481 EDTA, 1:200 Protease Inhibitor Cocktail (Sigma-Aldrich), 1 mM phenylmethylsulfonylfluoride
482 (Roche), and 1% octyl-beta-D glucopyranoside (Sigma-Aldrich) at 4°C for 1 hour, after
483 homogenization with an IKA T10 standard ULTRA TURRAX. Lysates were cleared by
484 centrifugation with a table-top centrifuge (Eppendorf Centrifuge) at 4°C at 20,000 g for 50 min.
485 MHC-I molecules purification was done with HB51 antibodies for C57BL/6 and a 1:1 mix of
486 HB51, HiB antibodies for C57BL/6; BALB/2c; 129_SvJae. Immunoprecipitations in 96-well
487 plates followed the protocol of [45]. Shortly, after plate conditioning, cross-linked beads and then
488 lysates were added to single wells, followed by washes at different sodium chloride
489 concentrations and an acidic elution step. Peptides were then desalted and purified on C18-
490 columns. Recovered peptides were dried using vacuum centrifugation (Thermo Fisher
491 Scientific) and stored at -80°C.

492 **Mass-spectrometry acquisition**

493 For Mass spectrometry (MS) analysis, MHC-I peptide samples were resuspended in 8 µl of
494 2% ACN and 0.1% formic acid (FA). 3 µl of peptide resuspension was injected into the LC-MS
495 setup per measurement, counting two in DDA and one in DIA. The LC-MS setup consists of
496 an Easy-nLC 1200 (Thermo Fisher Scientific) connected to a Q Exactive HF-X (Thermo Fisher
497 Scientific). Chromatographic separation was done with a 450 mm homemade column of 75 µm
498 inner diameter packed with ReproSil Pur C18-AQ 1.9µm resin (Dr. Maisch GmbH). For DDA
499 measurements, the chromatographic separation was performed over 2 hours using a gradient
500 of H_2O:FA, 99.9%:0.1% (solvent A) and CH_3CN:FA 80%:0.1% (solvent B). The gradient
501 consisted of sequential, linear steps: 0 to 110 min (2-25% B), 110 to 114 min (25-35% B), 114
502 to 115 min (35-100% B), and 115 to 120 min (constant at 100% B) at a flow rate of 250 nl/min.
503 The mass spectrometer had the following parameters set: full-scan MS spectra were acquired
504 from m/z = 300-1,650 at a resolution of 60,000 (m/z = 200) with maximum injection times of 80
505 ms. Auto gain control (AGC) target value was tuned to 3 x 10^6 ions. We acquired MS/MS
506 spectra at a resolution of 30,000 (m/z = 200), a top 20 method and isolation windows of 1.2
507 m/z, as well as a collision energy of 27 (HCD). All MS/MS scans accumulated ions to an AGC
508 target value of 2 x 10^5 at a maximum injection time of 120 ms. Precursors of charge 4 and
509 above were not selected for fragmentation. The dynamic exclusion was set to 20s. For DIA,
510 the chromatographic separation was performed as in DDA measurements. The DIA acquisition
511 cycles included one full-scan MS spectra, acquired from m/z = 300-1,650 (Resolution =
512 120,000, ion accumulation time = 60 ms), and 22 MS/MS scans. For all MS/MS scans the AGC
513 target value was set to 3 x 10^6 ion, mass resolution at 30,000 and a stepped normalized
514 collision energy (25.5, 27, 30) was applied. The maximum ion accumulation was set to auto
515 and their first mass was fixed to 200 m/z. Consecutive MS/MS scans overlapped in their m/z
516 windows by 1 m/z.

517 **Immunopeptidomics data processing**

518 All DDA files were used to generate a library with a database search using FragPipe (v22.0),
519 including MSFragger (v4.1) [46]. The FASTA file was compiled as described in 'Ribosome
520 profiling data analysis'. For search space generation, unspecific digestion with peptide lengths
521 of 8 to 14 amino acids was used. Variable modifications included methionine oxidation, N-
522 terminal acetylation, and cysteine carbamidomethylation. No fixed modifications were applied.
523 Peptide, ion, and psm FDRs were set to 0.03 while applying a group-specific FDR as indicated
524 in the FASTA header with PE = X, X being the respective protein group. No protein FDR was
525 applied. All other settings were set to default. DIA files were searched with the library described
526 above using DIA-NN (v1.8) with a precursor q-value cut-off of 0.01. Peptide binding affinities
527 were predicted with MixMHC [47]. Peptides were considered as binders when they had a %-rank

528 below 2 for at least one HLA allele present in the sample haplotypes. Data analyses were done
529 with Julia and R, visualizations with R.

530 **Protein extraction and Western Blot**

531 Total proteins from mouse liver samples were isolated according to the NUN (NaCl, Urea,
532 Nonidet P-40) procedure, as [16]: Livers were homogenized in two tissue volumes of 10 mM
533 Hepes (pH 7.6), 100 mM KCl, 0.1 mM EDTA, 10% glycerol, 0.15 mM spermine, and 0.5 mM
534 spermidine for 15 s using a Teflon homogenizer. Four tissue volumes of 2x NUN buffer (2 M
535 urea, 2% NP-40, 0.6 M NaCl, 50 mM Hepes [pH 7.6], 2 mM dithiothreitol, and 0.1 mM
536 phenylmethylsulfonyl fluoride; supplemented with complete protease inhibitor tablets, Roche)
537 were added dropwise on a vortex with low speed. Lysates were incubated 1 h on ice and
538 cleared through centrifugation at 10,000 rpm, 4°C, for 20 min. Aliquots of the lysates (40 µg of
539 protein loaded per lane) were separated by SDS-polyacrylamide gel electrophoresis and
540 transferred to PVDF membrane using an iBlot 2 gel transfer device. The membrane was
541 blocked using 5% milk in Tris-buffered saline with 0,1% Tween 20 (TBST), 1 h at RT, followed
542 by an incubation overnight at 4°C with appropriate dilutions of primary antibodies, including
543 anti-Cleaved CASPASE3 (Cell Signaling Technology, 9661), anti-MDA5 (Cell Signaling
544 Technology, 5321), anti-PTEN (Cell Signaling Technology, 9188), anti-Hamartin/TSC1 (Cell
545 Signaling Technology, 6935), anti-GAPDH (Cell Signaling Technology, 2118), and anti-
546 VINCULIN (Abcam, ab129002). Following TBST washing (5 min, three times), the membrane
547 was incubated with the appropriate secondary antibody conjugated with horseradish
548 peroxidase for 60 min at RT, followed by TBST washing (15 min, three times).
549 Chemiluminescence signal was detected using Supersignal West Femto Maximum Sensitivity
550 Substrate (Thermofisher Scientific, 34095), as described by the manufacturer. The
551 quantification of signal was performed using ImageJ software.

552 **Deletion of *Ifih1* in *Smg6*$^{flox/flox}$; *CreERT2* fibroblasts via CRISPR**

553 First, lentiCRISPRv2-Blast-mU6 empty backbone (kind gift from J. Van Leeuwen, Addgene
554 plasmid #206806) [48] was digested with BsmBI (NEB, 0580) enzyme. The digestion products
555 were run on an agarose gel (0.8%), and the band corresponding to the open vector (~11 kb)
556 was excised, followed by DNA purification using QIAquick Gel Extraction Kit. Following
557 annealing reaction was assembled in a tube: 1 µl Forward primer (100 µM), 1 µl Reverse primer
558 (100 µM), 1 µl 10x T4 ligation buffer (NEB, B0202S), 0.5 µl T4 PNK (NEB, B0201S), and 6.5
559 µl H_2O. Primers were annealed with the following protocol: incubate 30 min at 37°C, and 5 min
560 at 95°C, respectively, then cool to 25°C at a rate of 5°C/min. Annealed primers were ligated
561 into the open vector using the following mixture: 50 ng open vector, 2 µl 10x T4 ligation buffer,
562 1 µl T4 DNA ligase (NEB, M0202S), 1 µl annealed primers (1:100 diluted), and nuclease-free

563 H_2O to 20 µl. Ligation mix was incubated at RT for 1 h. 10 µl ligation mix was added to 100 µl
564 Stbl3 competent cells, and incubated on ice for 30 min, followed by a heat-shock for 30 sec at
565 42°C. After a short incubation (5 min, on ice), 1 ml S.O.C. medium was added to the mixture,
566 and the tube was incubated at 37°C, for 1 h with shaking. 100 µl of the transformation mixture
567 was plated on an agar plate containing Ampicillin and incubated overnight at 37°C. Positive
568 colonies were selected and cultured overnight with shaking at 37°C, in LB medium containing
569 Ampicillin, then purified using a Midiprep kit (QIAGEN, 12943). Cells were transfected with the
570 plasmid using Lipofectamine 3000 (Thermo Fisher Scientific, L3000001), according to the
571 manufacturer's protocol, for 24 h, then were selected with Blasticidin (5 µg/ml) for 96 h. *Ifih1*$^{ko/ko}$
572 cells were obtained through single cell cloning. *Ifih1* sgRNA primer sequences: forward, CAC
573 CGC GTA GAC GAC ATA TTA CCA G; reverse, AAA CCT GGT AAT ATG TCG TCT ACG C.

574 **Induction of Cre-mediated recombination in fibroblasts**

575 Two different methods were used to induce Cre-dependent recombination:
576 1-Direct delivery of recombinant CRE protein (TAT-CRE, kind gift from I. Lopez-Mejia)*:*
577 *Smg6*$^{w/wt}$ and *Smg6*$^{flox/flox}$ (-/+ *Ifih1*$^{ko/ko}$) fibroblasts were seeded in 6-well plates. The standard
578 culture medium (Thermo Fisher Scientific, 41965062) was replaced with Opti-MeM (Thermo
579 Fisher Scientific, 31985062). Cells were subsequently treated with 2.5 µM TAT-CRE or vehicle
580 for 8 h. After treatment, OptiMeM was replaced with the standard culture medium.
581 2-Recombination via 4-hydroxytamoxifen (4-OHT): *Smg6*$^{flox/flox}$; *CreERT2* cells were treated
582 with 2 µM 4-OHT or DMSO for 3 days (4-OHT containing media was refreshed every 24 h).
583 In both methods, cells were maintained in culture for at least one-week post-treatment to
584 ensure efficient recombination. Cells were subsequently collected for RNA extraction (as
585 explained above).

586 **J2 immunofluorescence**

587 Immunofluorescence of dsRNA was performed as [49]. First, *Smg6*$^{flox/flox}$ cells were seeded in a
588 6-well plate, then treated with 2.5 µM TAT-CRE or vehicle as above. One week after the
589 treatment, cells were transferred to a new 6-well plate containing coverslips, at a confluency
590 of ca. 20%. Next day, the culture medium was removed, and cells were fixed using 4%
591 paraformaldehyde (PFA) for 15 min at RT, then washed three times (5 min each time), with 1x
592 PBS. Fixed cells were permeabilized with 500 µl PBSTX, followed by a 10 min incubation at
593 RT. PBSTX was removed, 500 µl of IFA blocking buffer was added into each well, and
594 incubated for 1 h, at RT with rocking. After blocking, cells were incubated with 500 µl primary
595 antibody solution (anti-dsRNA monoclonal antibody J2: Jena Bioscience, RNT-SCI-10010200)
596 in IFA blocking buffer (1:1000), overnight, at 4°C with rocking. Primary antibody solution was
597 removed, and cells were washed with 500 µl PBSTX (three times, for 5 min each). Cells were

598 incubated with the secondary antibody solution in PBSTX (1:300, Goat anti-mouse IgG Alexa
599 Fluor 488 for detection of J2, followed by washes with 500 µl PBSTX 3 times, for 5 min each).
600 To prepare the slides for imaging, coverslips were removed from 6-well plate, and cleaned with
601 70% ethanol, then placed face down onto the glasses, sealed with a nail polish. Images were
602 captured using a fluorescence microscope. The quantification of J2 intensity was performed
603 on ImageJ software.

604 **Enzyme-linked immunosorbent assay (ELISA)**

605 CXCL10 ELISA (R&D, DY466) was performed using R&D DuoSet™ ELISA development
606 system, according to manufacturer's protocol. 96-well ELISA plate (R&D, DY990) was coated
607 with 100 µl of capture antibody solution and incubated overnight at room temperature.
608 Following washes using wash buffer (R&D, WA126) three times, plate was blocked with 300
609 µl block buffer (R&D, DY995) for 1 hour at room temperature. Washes were repeated as above.
610 100 µl of diluted samples and standards were added to the plate and then incubated for 2
611 hours at room temperature. Washes were repeated as above. 100 µl of detection antibody
612 solution was added to the plate and then incubated for 2 hours at room temperature. Washes
613 were repeated as above. 100 µl of Streptavidin-HRP B solution was added to the plate and
614 then incubated for 20 minutes at room temperature. Washes were repeated as above. 100 µl
615 of substrate solution (R&D, DY999B) was added to the plate and then incubated for 20 minutes
616 at room temperature. The reaction was stopped via stopping solution (R&D, DY994). Protein
617 levels were detected using a microplate reader at 450 nm optical density.

618 **Ex vivo peptide stimulation of leukocytes**

619 Intrahepatic leukocytes isolated from mice as explained above. Spleens were mechanically
620 disrupted and filtered through a 70 µm cell strain to obtain single-cell suspensions. Both
621 intrahepatic leukocytes and spleens were washed with PBS. 2 million cells per mouse per
622 condition were seeded in round-bottom 96-well plates in T-cell medium (RPMI supplemented
623 with 25 µM 2-mercaptoethanol, 1 mM sodium pyruvate, MEM non-essential amino acids
624 (Gibco™, 11140050), 10% FBS, 1% Penicillin/Streptomycin, and L-glutamine. A pool of non-
625 canonical, canonical, and common peptides was added to the appropriate wells at a final
626 concentration of 2 µg/ml per peptide. CD28 agonist antibody (1 µg/ml; BioLegend, 102115)
627 and Brefeldin A were added to all wells. Cells were incubated at 37°C for 8 hours. After
628 incubation, cells were collected and stained with Zombie UV™ Fixable Viability Kit (1:500;
629 BioLegend, 423107) to stain dead cells. Then, extracellular and intracellular staining was
630 performed using BD Cytofix/Cytoperm™ Fixation/Permeabilization Kit (Cat# 554714)
631 according to the manufacturer's instructions. Data were acquired on a BD LSR Fortessa flow
632 cytometer and analyzed using FlowJo software. Antibodies used were: CD3-PE (BioLegend,

633 100206), CD45-Pacific Blue (BioLegend, 103126), CD8a-Brilliant Violet 510 (BioLegend,
634 100714), and IFNγ-APC (BioLegend, 505810).

635 **RNA structure prediction**

636 RNA structure prediction was performed via RNAfold web server using default parameters
637 (http://rna.tbi.univie.ac.at/cgi-bin/RNAWebSuite/RNAfold.cgi).

638 **Repetitive element analysis**

639 Repetitive elements within individual transcripts were detected using RepeatMasker [50] web
640 server (https://www.repeatmasker.org/cgi-bin/WEBRepeatMasker).

641 **Acknowledgements**

642 We thank the Lausanne Genomic Technologies Facility for library preparation and sequencing,
643 University of Lausanne Peptide & Tetramer Core Facility for the synthesis of synthetic
644 peptides, F. Lammers for help with genotyping, C. Roger for histology analysis, G.
645 Niederhäuser for serum measurements, Anne-Claire Godet at www.threoninedesign.fr for the
646 graphical illustration in Figure 5g, I. Lopez-Mejia for providing TAT-CRE, J. Van Leeuwen for
647 providing lentiCRISPRv2-Blast-mU6 plasmid, M. Hall and D. Mossmann for providing L-dKO
648 mice and for scientific inputs, O. Mühlemann and E. Karousis for important discussions. D.G.
649 acknowledges funding by Swiss National Science Foundation (SNSF) NCCR RNA & Disease
650 Phase III funding (grant number 205601), SNSF project grant (212423) and by Novartis
651 Foundation for Medical-Biological Research grant (21B066).

652 **Author Contributions**

653 Conceptualization: E.S.A. and D.G.; methodology: E.S.A., V.R., I.E.S., M.J., Y.M., L.B., I.G.-
654 M., and A.P.B.; investigation: E.S.A., V.R., I.E.S., M.J., Y.M., I.G.-M., and L.Q.-M.;
655 visualization: E.S.A., V.R., I.E.S., M.J., Y.M., and I.G.-M.; supervision: D.G., L.Q.-M., J.R.,
656 T.V.P., S.A.L., and M.B.-S.; writing: E.S.A. and D.G.

657 **Declaration of Interests**

658 The authors declare no competing interests.

659 **Data Availability**

660 The transcriptomics and ribo-seq data discussed in this publication have been deposited in
661 NCBI's Gene Expression Omnibus [51] and are accessible through GEO Series accession
662 numbers GSE278996 and GSE278997. The mass spectrometry proteomics data have been

663 deposited to the ProteomeXchange Consortium via the PRIDE [52] partner repository with the
664 dataset identifier PXD057903.

665 **Code Availability**

666 All computational scripts are available on GitHub (https://github.com/NMD_Smg6/).

667 **References**

668 1. Kurosaki, T., Popp, M.W. & Maquat, L.E. Quality and quantity control of gene
669 expression by nonsense-mediated mRNA decay. *Nature reviews. Molecular cell biology*
670 **20**, 406-420 (2019).
671 2. Karousis, E.D. & Muhlemann, O. The broader sense of nonsense. *Trends Biochem Sci*
672 **47**, 921-935 (2022).
673 3. Boehm, V. *et al.* SMG5-SMG7 authorize nonsense-mediated mRNA decay by enabling
674 SMG6 endonucleolytic activity. *Nature communications* **12**, 3965 (2021).
675 4. Supek, F., Lehner, B. & Lindeboom, R.G. To NMD or Not To NMD: nonsense-
676 mediated mRNA decay in cancer and other genetic diseases. *Trends in Genetics* **37**,
677 657-668 (2021).
678 5. Lindeboom, R.G.H., Vermeulen, M., Lehner, B. & Supek, F. The impact of nonsense-
679 mediated mRNA decay on genetic disease, gene editing and cancer immunotherapy.
680 *Nat Genet* **51**, 1645-1651 (2019).
681 6. Wu, C.C. *et al.* Immuno-genomic landscape of osteosarcoma. *Nat Commun* **11**, 1008
682 (2020).
683 7. Litchfield, K. *et al.* Escape from nonsense-mediated decay associates with anti-tumor
684 immunogenicity. *Nat Commun* **11**, 3800 (2020).
685 8. Oka, M. *et al.* Aberrant splicing isoforms detected by full-length transcriptome
686 sequencing as transcripts of potential neoantigens in non-small cell lung cancer.
687 *Genome Biol* **22**, 9 (2021).
688 9. Becker, J.P. *et al.* NMD inhibition by 5-azacytidine augments presentation of
689 immunogenic frameshift-derived neoepitopes. *iScience* **24**, 102389 (2021).
690 10. Zhang, Y. *et al.* Immunotherapy for breast cancer using EpCAM aptamer tumor-
691 targeted gene knockdown. *Proc Natl Acad Sci U S A* **118** (2021).
692 11. Pastor, F., Kolonias, D., Giangrande, P.H. & Gilboa, E. Induction of tumour immunity
693 by targeted inhibition of nonsense-mediated mRNA decay. *Nature* **465**, 227-230 (2010).
694 12. Meraviglia-Crivelli, D. *et al.* IL-6/STAT3 signaling in tumor cells restricts the
695 expression of frameshift-derived neoantigens by SMG1 induction. *Mol Cancer* **21**, 211
696 (2022).
697 13. Meraviglia-Crivelli, D. *et al.* A pan-tumor-siRNA aptamer chimera to block nonsense-
698 mediated mRNA decay inflames and suppresses tumor progression. *Mol Ther Nucleic*
699 *Acids* **29**, 413-425 (2022).
700 14. Nasif, S. *et al.* Inhibition of nonsense-mediated mRNA decay reduces the
701 tumorigenicity of human fibrosarcoma cells. *NAR Cancer* **5**, zcad048 (2023).
702 15. Hwang, J. & Maquat, L.E. Nonsense-mediated mRNA decay (NMD) in animal
703 embryogenesis: to die or not to die, that is the question. *Curr Opin Genet Dev* **21**, 422-
704 430 (2011).
705 16. Katsioudi, G. *et al.* A conditional Smg6 mutant mouse model reveals circadian clock
706 regulation through the nonsense-mediated mRNA decay pathway. *Science advances* **9**,
707 eade2828 (2023).
708 17. Guri, Y. *et al.* mTORC2 Promotes Tumorigenesis via Lipid Synthesis. *Cancer Cell* **32**,
709 807-823 e812 (2017).
710 18. Li, T. *et al.* Smg6/Est1 licenses embryonic stem cell differentiation via nonsense-
711 mediated mRNA decay. *The EMBO journal* **34**, 1630-1647 (2015).
712 19. Postic, C. & Girard, J. The role of the lipogenic pathway in the development of hepatic
713 steatosis. *Diabetes Metab* **34**, 643-648 (2008).

714 20. Snoek, M., van Dinten, L. & van Vugt, H. A novel gene, G7e, resembling a viral
715 envelope gene, is located at the recombinational hot spot in the class III region of the
716 mouse MHC. *Genomics* **38**, 5-12 (1996).
717 21. Du, N.H., Arpat, A.B., De Matos, M. & Gatfield, D. MicroRNAs shape circadian
718 hepatic gene expression on a transcriptome-wide scale. *eLife* **3**, e02510 (2014).
719 22. Schoggins, J.W. *et al.* A diverse range of gene products are effectors of the type I
720 interferon antiviral response. *Nature* **472**, 481-485 (2011).
721 23. Sung, J.H. *et al.* Chemokine guidance of central memory T cells is critical for antiviral
722 recall responses in lymph nodes. *Cell* **150**, 1249-1263 (2012).
723 24. Bowling, E.A. *et al.* Spliceosome-targeted therapies trigger an antiviral immune
724 response in triple-negative breast cancer. *Cell* **184**, 384-403 e321 (2021).
725 25. Zheng, R. *et al.* hnRNPM protects against the dsRNA-mediated interferon response by
726 repressing LINE-associated cryptic splicing. *Mol Cell* **84**, 2087-2103 e2088 (2024).
727 26. Dias Junior, A.G., Sampaio, N.G. & Rehwinkel, J. A Balancing Act: MDA5 in Antiviral
728 Immunity and Autoinflammation. *Trends Microbiol* **27**, 75-85 (2019).
729 27. Lewis, B.P., Green, R.E. & Brenner, S.E. Evidence for the widespread coupling of
730 alternative splicing and nonsense-mediated mRNA decay in humans. *Proceedings of*
731 *the National Academy of Sciences* **100**, 189-192 (2003).
732 28. Zhou, H. & Deng, X.W. Intron Retention, an Orchestrated Program of Gene Expression
733 Regulation. *Bioessays* **47**, e202400248 (2025).
734 29. Rehwinkel, J. & Gack, M.U. RIG-I-like receptors: their regulation and roles in RNA
735 sensing. *Nat Rev Immunol* **20**, 537-551 (2020).
736 30. Pichlmair, A. *et al.* Activation of MDA5 requires higher-order RNA structures
737 generated during virus infection. *J Virol* **83**, 10761-10769 (2009).
738 31. Schonborn, J. *et al.* Monoclonal antibodies to double-stranded RNA as probes of RNA
739 structure in crude nucleic acid extracts. *Nucleic Acids Res* **19**, 2993-3000 (1991).
740 32. Pepin, G. *et al.* Cre-dependent DNA recombination activates a STING-dependent innate
741 immune response. *Nucleic Acids Res* **44**, 5356-5364 (2016).
742 33. Rehwinkel, J. & Mehdipour, P. ADAR1: from basic mechanisms to inhibitors. *Trends*
743 *Cell Biol* **35**, 59-73 (2025).
744 34. Rigby, R.E. & Rehwinkel, J. RNA degradation in antiviral immunity and autoimmunity.
745 *Trends Immunol* **36**, 179-188 (2015).
746 35. Schuler, M., Dierich, A., Chambon, P. & Metzger, D. Efficient temporally controlled
747 targeted somatic mutagenesis in hepatocytes of the mouse. *Genesis* **39**, 167-172 (2004).
748 36. Horie, Y. *et al.* Hepatocyte-specific Pten deficiency results in steatohepatitis and
749 hepatocellular carcinomas. *J Clin Invest* **113**, 1774-1783 (2004).
750 37. Kwiatkowski, D.J. *et al.* A mouse model of TSC1 reveals sex-dependent lethality from
751 liver hemangiomas, and up-regulation of p70S6 kinase activity in Tsc1 null cells. *Hum*
752 *Mol Genet* **11**, 525-534 (2002).
753 38. Benechet, A.P. *et al.* Dynamics and genomic landscape of CD8(+) T cells undergoing
754 hepatic priming. *Nature* **574**, 200-205 (2019).
755 39. Gatfield, D. *et al.* Integration of microRNA miR-122 in hepatic circadian gene
756 expression. *Genes Dev* **23**, 1313-1326 (2009).
757 40. Dobin, A. *et al.* STAR: ultrafast universal RNA-seq aligner. *Bioinformatics* **29**, 15-21
758 (2013).
759 41. Love, M.I., Huber, W. & Anders, S. Moderated estimation of fold change and dispersion
760 for RNA-seq data with DESeq2. *Genome Biol* **15**, 550 (2014).
761 42. Snieckute, G. *et al.* ROS-induced ribosome impairment underlies ZAKalpha-mediated
762 metabolic decline in obesity and aging. *Science* **382**, eadf3208 (2023).

763 43. Martin, M. Cutadapt removes adapter sequences from high-throughput sequencing
764 reads. *EMBnet.journal* **17**, 10-12 (2011).
765 44. Lawrence, M. *et al.* Software for computing and annotating genomic ranges. *PLoS*
766 *Comput Biol* **9**, e1003118 (2013).
767 45. Chong, C. *et al.* High-throughput and Sensitive Immunopeptidomics Platform Reveals
768 Profound Interferongamma-Mediated Remodeling of the Human Leukocyte Antigen
769 (HLA) Ligandome. *Mol Cell Proteomics* **17**, 533-548 (2018).
770 46. Kong, A.T., Leprevost, F.V., Avtonomov, D.M., Mellacheruvu, D. & Nesvizhskii, A.I.
771 MSFragger: ultrafast and comprehensive peptide identification in mass spectrometry-
772 based proteomics. *Nat Methods* **14**, 513-520 (2017).
773 47. Gfeller, D. *et al.* Improved predictions of antigen presentation and TCR recognition
774 with MixMHCpred2.2 and PRIME2.0 reveal potent SARS-CoV-2 CD8(+) T-cell
775 epitopes. *Cell Syst* **14**, 72-83 e75 (2023).
776 48. Unlu, B. *et al.* Global analysis of suppressor mutations that rescue human genetic
777 defects. *Genome Med* **15**, 78 (2023).
778 49. de Faria, I.J.S., Imler, J.L. & Marques, J.T. Protocol for the analysis of double-stranded
779 RNAs in virus-infected insect cells using anti-dsRNA antibodies. *STAR Protoc* **4**,
780 102033 (2023).
781 50. Smit, A., Hubley, R. & Green, P. RepeatMasker Open-3.0.
782 **http://www.repeatmasker.org** (1996-2004).
783 51. Edgar, R., Domrachev, M. & Lash, A.E. Gene Expression Omnibus: NCBI gene
784 expression and hybridization array data repository. *Nucleic Acids Res* **30**, 207-210
785 (2002).
786 52. Perez-Riverol, Y. *et al.* The PRIDE database resources in 2022: a hub for mass
787 spectrometry-based proteomics evidences. *Nucleic Acids Res* **50**, D543-D552 (2022).

Figures and Figure Legends

Arpa et al. Figure 1

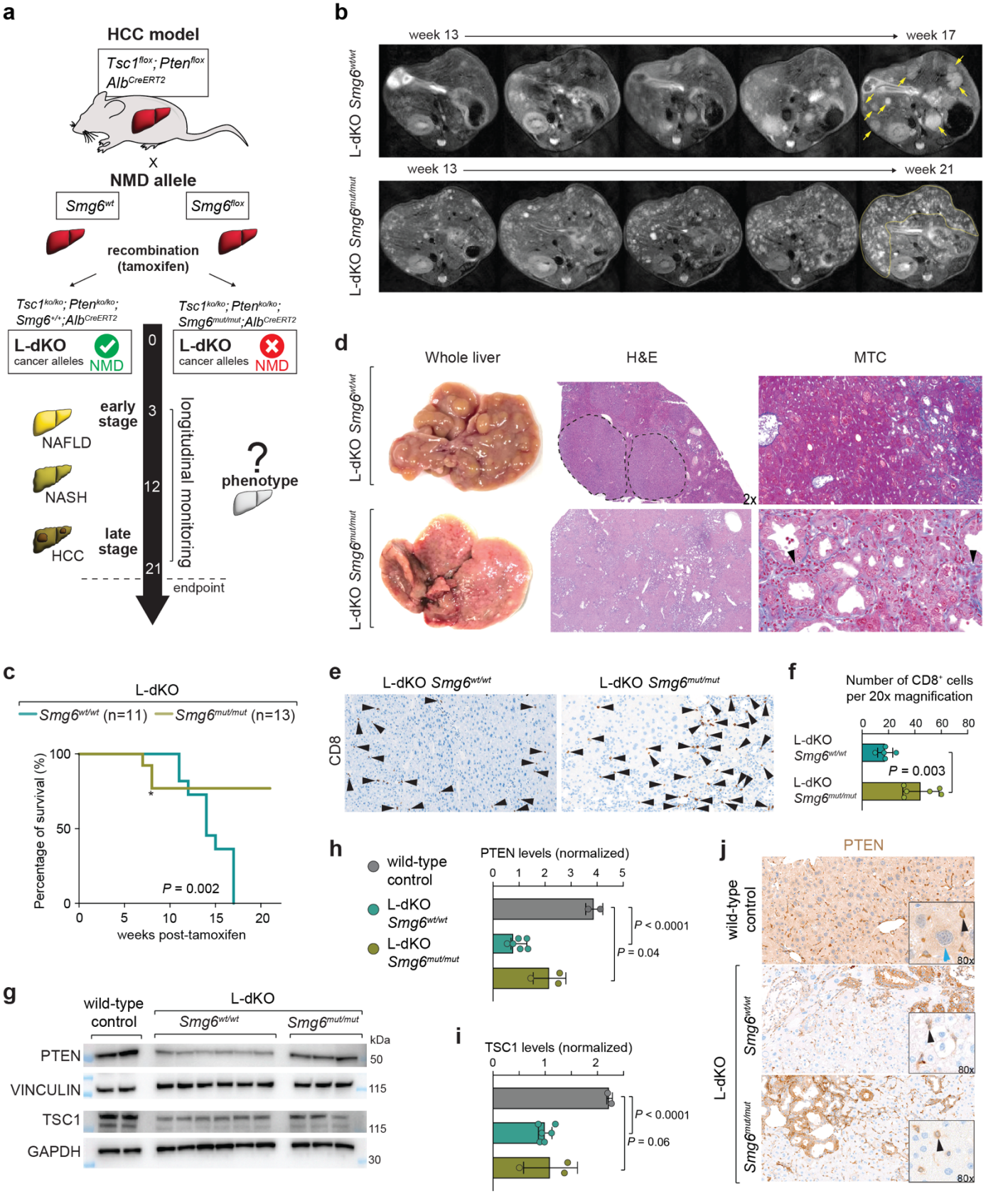

Figure 1. *Smg6* mutation suppresses cancer in genetic HCC model.

(a) Schematic of the experimental design. Inactivation of tumor suppressor genes *Tsc1* and *Pten* via Cre-mediated recombination in liver (L-dKO) leads to tumors/HCC from week 12 [17]. Cre-mediated recombination of the *Smg6*^{flox} allele to *Smg6*^{mut} introduces point mutations in catalytically important residues of the PIN domain [16]. Both L-dKO *Smg6*$^{wt/wt}$ and *Smg6*$^{flox/flox}$ mice received 4 intraperitoneal tamoxifen injections to activate hepatocyte-specific CreERT2 (driven from *Albumin* promoter). Early-stage experiments were conducted 3 weeks post-tamoxifen. Late-stage animals were scanned via MRI from week 12 to 21 (endpoint). In L-dKO *Smg6*$^{wt/wt}$, livers show NAFLD and NASH as indicated.

(b) Representative longitudinal MRI scans for a tumor-bearing L-dKO *Smg6*^{wt} mouse (top) and a tumor-free L-dKO *Smg6*^{mut} animal. Tumors in L-dKO *Smg6*^{wt} liver are indicated with yellow arrows (upper). Fibrotic plaques marked by yellow line in L-dKO *Smg6*^{mut} liver (lower).

(c) Kaplan-Meier plot, from two different cohorts, displays survival percentage of L-dKO *Smg6*^{wt} (n = 11) and *Smg6*^{mut} (n = 13) mice throughout the experiment. *P*-value by a log-rank (Mantel-Cox) test. Asterisk indicates 3 animals that deceased for other reasons than HCC in one of the cohorts (stress in animal handling).

(d) Representative whole liver images, Masson's Trichrome (MTC) staining for fibrosis (at 20x magnification) and H&E images (at 2x magnification) from late-stage L-dKO *Smg6*^{wt} and *Smg6*^{mut} mice. Dashed lines surround tumors in L-dKO *Smg6*^{wt}. Arrowheads indicate fibrotic areas in L-dKO *Smg6*^{mut}.

(e) Representative immunohistochemistry (IHC) images of livers from late-stage mice, showing CD8-positive cells, at 20x magnification. Arrowheads mark CD8+ T-cells (brown).

(f) Quantification of CD8 IHC images. For each sample, the number of CD8-positive T-cells was counted in 15 randomly selected images, at 20x magnification (L-dKO *Smg6*^{wt}, n = 5 mice; L-dKO *Smg6*^{mut}, n = 6 mice). The *P*-value was calculated with two-tailed unpaired *t*-test.

(g) Western blot analysis of total liver proteins from late-stage mice for PTEN and TSC1. VINCULIN and GAPDH served as loading controls (Control, n = 2 mice; L-dKO *Smg6*^{wt}, n = 6 mice; L-dKO *Smg6*^{mut}, n = 3 mice).

(h) Quantification of PTEN and VINCULIN Western blots from (g)

(i) Quantification of TSC1 and GAPDH Western blots from (g).

(j) Representative IHC images of livers from late-stage mice stained with anti-PTEN antibodies. Light brown staining shows PTEN expression in hepatocytes in wild-type

control (blue arrowhead). Dark brown staining indicates PTEN expression in non-hepatocyte cells in both wild-type control and L-dKO (black arrowhead). Images were captured at 20x (large images) and 80x (small images) magnifications.

For (f), (h), and (i) data are plotted as means, and the error bars indicate SEM. The *P*-values were calculated with two-tailed unpaired *t*-test.

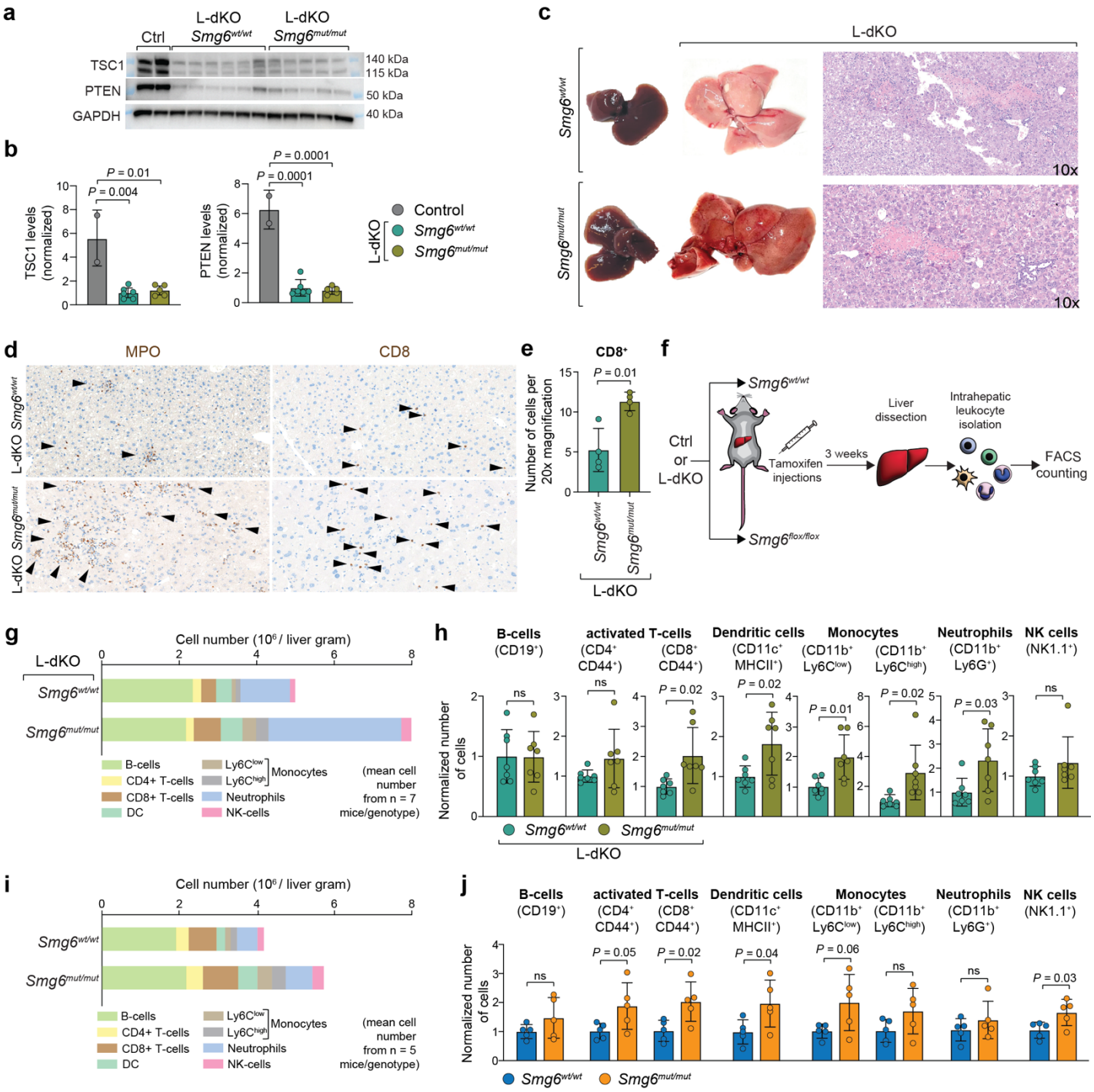
a
Ctrl
L-dKO Smg6wt/wt
L-dKO Smg6mut/mut
TSC1
PTEN
GAPDH
140 kDa
115 kDa
50 kDa
40 kDa
b
TSC1 levels (normalized)
PTEN levels (normalized)
P = 0.01
P = 0.004
P = 0.0001
P = 0.0001
Control
L-dKO
Smg6wt/wt
Smg6mut/mut
c
L-dKO
Smg6wt/wt
Smg6mut/mut
10x
10x
d
MPO
CD8
L-dKO Smg6wt/wt
L-dKO Smg6mut/mut
e
CD8+
Number of cells per 20x magnification
P = 0.01
Smg6wt/wt
Smg6mut/mut
L-dKO
f
Ctrl or L-dKO
Smg6wt/wt
Smg6flox/flox
Tamoxifen injections
3 weeks
Liver dissection
Intrahepatic leukocyte isolation
FACS counting
g
L-dKO
Cell number (10⁶ / liver gram)
Smg6wt/wt
Smg6mut/mut
B-cells
CD4+ T-cells
CD8+ T-cells
DC
Ly6Clow
Ly6Chigh
Monocytes
Neutrophils
NK-cells
(mean cell number from n = 7 mice/genotype)
h
B-cells (CD19+)
activated T-cells (CD4+ CD44+)
activated T-cells (CD8+ CD44+)
Dendritic cells (CD11c+ MHCII+)
Monocytes (CD11b+ Ly6Clow)
Monocytes (CD11b+ Ly6Chigh)
Neutrophils (CD11b+ Ly6G+)
NK cells (NK1.1+)
Normalized number of cells
ns
P = 0.02
P = 0.02
P = 0.01
P = 0.02
P = 0.03
ns
Smg6wt/wt
Smg6mut/mut
L-dKO
i
Cell number (10⁶ / liver gram)
Smg6wt/wt
Smg6mut/mut
B-cells
CD4+ T-cells
CD8+ T-cells
DC
Ly6Clow
Ly6Chigh
Monocytes
Neutrophils
NK-cells
(mean cell number from n = 5 mice/genotype)
j
B-cells (CD19+)
activated T-cells (CD4+ CD44+)
activated T-cells (CD8+ CD44+)
Dendritic cells (CD11c+ MHCII+)
Monocytes (CD11b+ Ly6Clow)
Monocytes (CD11b+ Ly6Chigh)
Neutrophils (CD11b+ Ly6G+)
NK cells (NK1.1+)
Normalized number of cells
ns
P = 0.05
P = 0.02
P = 0.04
P = 0.06
ns
ns
P = 0.03
Smg6wt/wt
Smg6mut/mut

Figure 2. SMG6-dependent early inflammation.

(a) Western blot analysis on total liver proteins, for PTEN and TSC1, at early-stage post-tamoxifen. GAPDH serves as loading control (Control, n = 2 mice; L-dKO *Smg6*^{wt}, n = 6 mice; L-dKO *Smg6*^{mut}, n = 5 mice).

(b) Quantification of Western blots from (a).

(c) Representative images of whole-livers from early-stage *Smg6*^{wt} and *Smg6*^{mut} mice, without and with L-dKO background, as well as Hematoxylin and Eosin (H&E)-stained sections (at 10x magnification) from early-stage L-dKO *Smg6*^{wt} and *Smg6*^{mut} mice.

(d) Representative IHC images of livers from early-stage L-dKO *Smg6*^{wt} and *Smg6*^{mut} mice, using neutrophil marker Myeloperoxidase (MPO) and T-cell marker CD8, at 20x magnification. Arrowheads mark MPO-positive or CD8-positive cells (brown).

(e) Quantification of CD8-stained IHC images. For each sample, the number of CD8+ T-cells was counted in 15 randomly selected images, at 20x magnification (mean values from 4 mice per group).

(f) Schematic of the experimental design for intrahepatic leukocyte isolation and flow cytometry-based counting. *Smg6*$^{wt/wt}$ and *Smg6*$^{flox/flox}$ mice (with or without L-dKO) received 5 intraperitoneal tamoxifen injections. Livers were dissected 3 weeks later, and leukocytes were isolated for flow cytometric quantification. FACS, fluorescence-associated cell sorting.

(g) Overall leukocyte numbers per gram liver tissue (mean values from 7 mice per group), as assessed by flow cytometry. Cells are identified according to indicated color code. DC, dendritic cells; NK-cells, natural killer cells.

(h) Relative leukocyte counts for individual cell types as assessed by flow cytometry. Graphs show normalized numbers (set to 1 in L-dKO *Smg6*$^{wt/wt}$) of indicated leukocyte type (n = 7 mice for each group).

(i) Overall leukocyte numbers per gram liver tissue (mean values from 5 mice per group), as assessed by flow cytometry. Cells are identified according to indicated color code.

(j) Relative leukocyte counts for individual cell types as assessed by flow cytometry. Graphs show normalized numbers (set to 1 in *Smg6*$^{wt/wt}$) of indicated leukocyte type (n = 5 mice for each group. Data are plotted as means, and the error bars indicate SEM.

For (b), (e), (h), and (j) data are plotted as means, and the error bars indicate SEM. The *P*-values were calculated with two-tailed unpaired *t*-test.

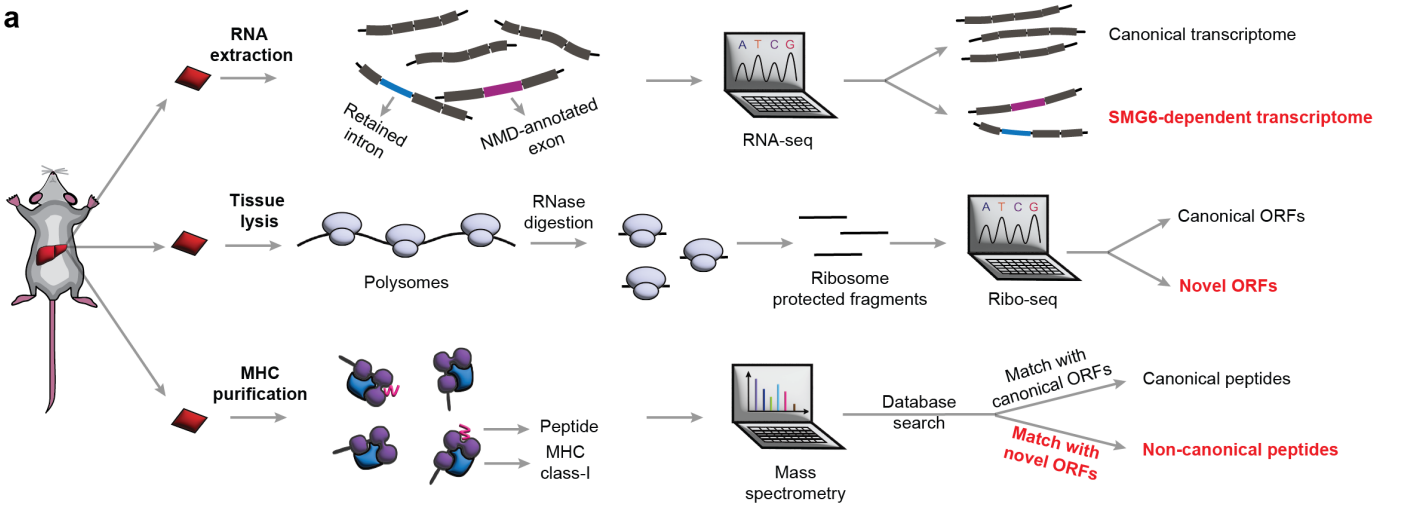
a
RNA extraction
Retained intron
NMD-annotated exon
RNA-seq
Canonical transcriptome
SMG6-dependent transcriptome
Tissue lysis
Polysomes
RNase digestion
Ribosome protected fragments
Ribo-seq
Canonical ORFs
Novel ORFs
MHC purification
Peptide MHC class-I
Mass spectrometry
Database search
Match with canonical ORFs
Match with novel ORFs
Canonical peptides
Non-canonical peptides

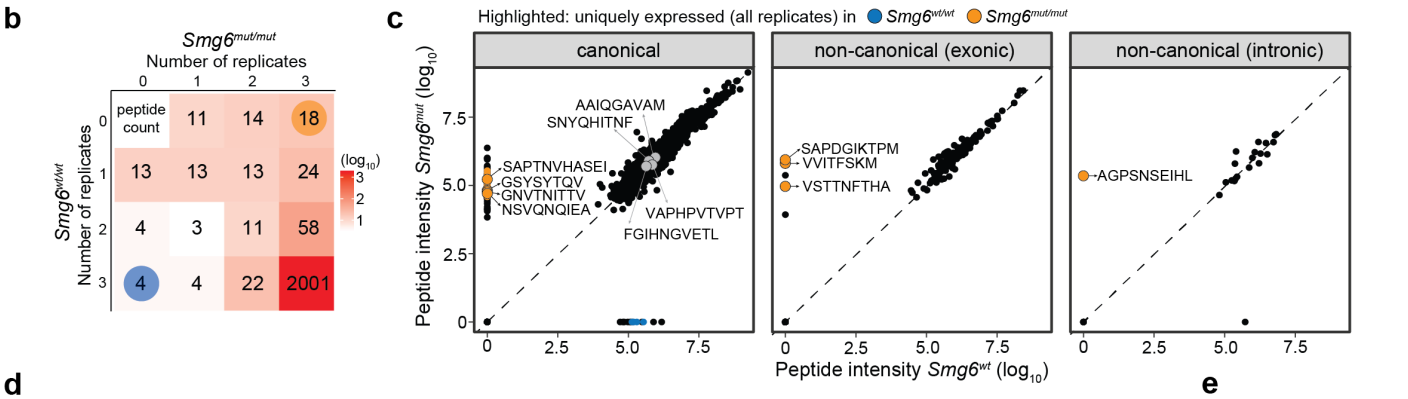
b
Smg6mut/mut
Number of replicates
Smg6wt/wt
Number of replicates
peptide count
11 14 18
13 13 13 24
4 3 11 58
4 4 22 2001
(log10)
c
Highlighted: uniquely expressed (all replicates) in Smg6wt/wt Smg6mut/mut
canonical
non-canonical (exonic)
non-canonical (intronic)
Peptide intensity Smg6mut (log10)
Peptide intensity Smg6wt (log10)
AAIQGAVAM
SNYQHITNF
SAPTNVHASEI
GSYSYTQV
GNVTNITTV
NSVQNQIEA
VAPHPVTVPT
FGIHNGVETL
SAPDGIKTPM
VVITFSKM
VSTTNFTHA
AGPSNSEIHL

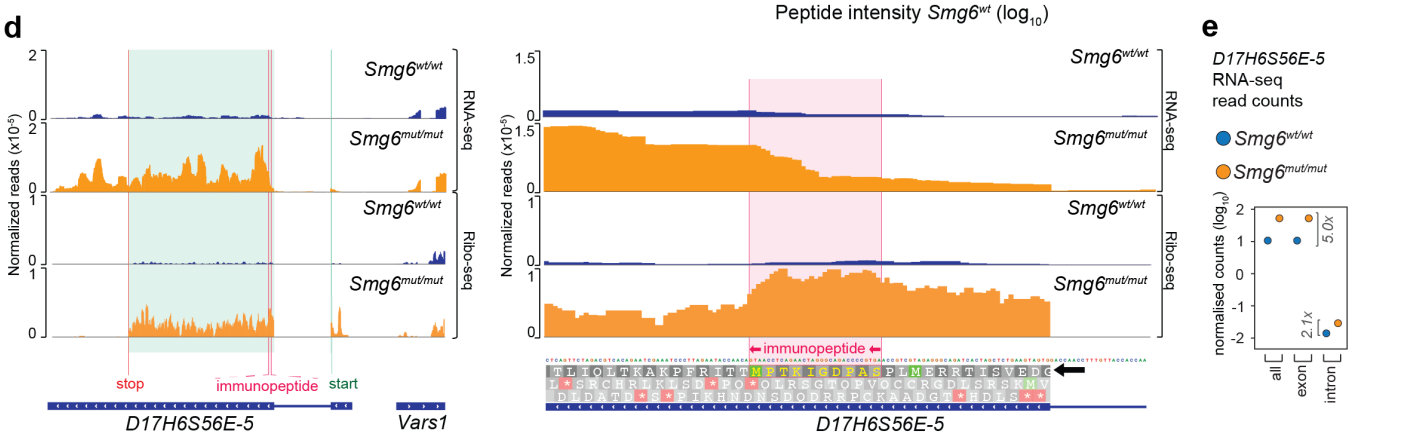
d
Normalized reads (x10-5)
Smg6wt/wt
Smg6mut/mut
RNA-seq
Ribo-seq
stop
immunopeptide
start
D17H6S56E-5
Vars1
e
D17H6S56E-5
RNA-seq
read counts
normalised counts (log10)
5.0x
2.1x
all
exon
intron

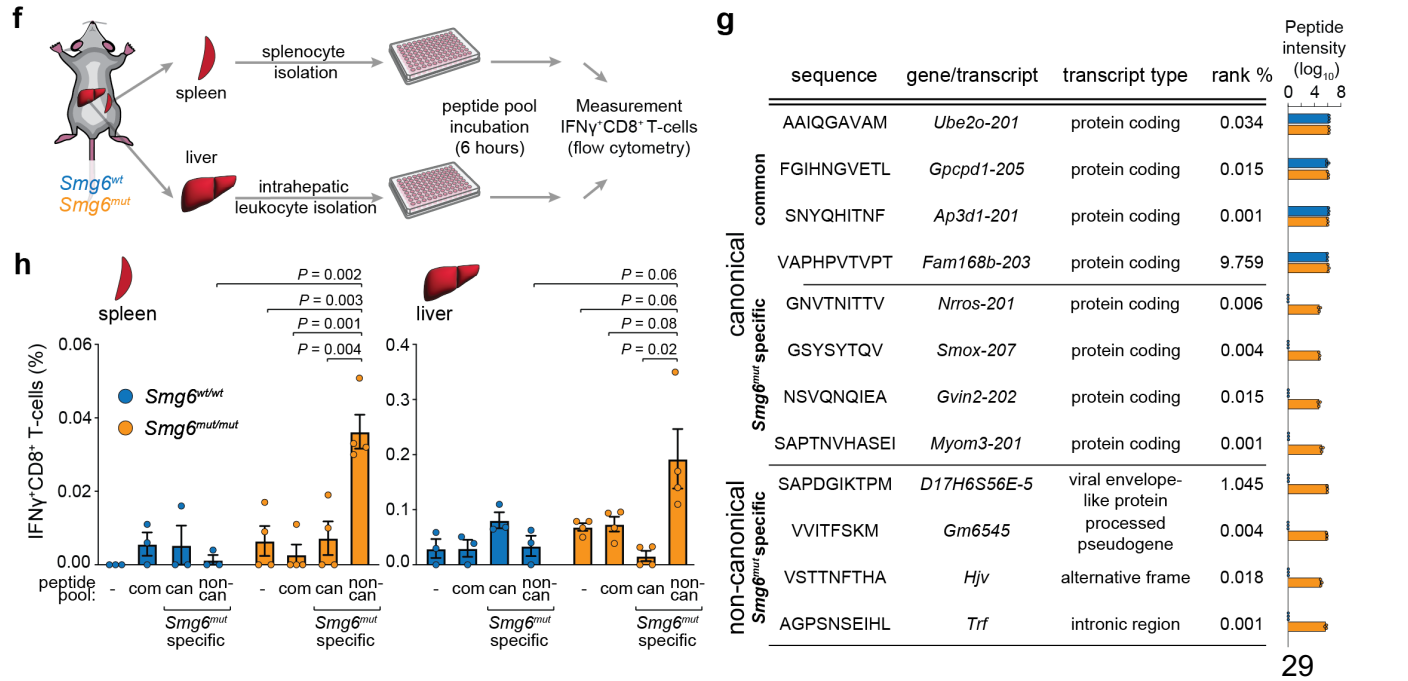
f
spleen
splenocyte isolation
liver
intrahepatic leukocyte isolation
peptide pool incubation (6 hours)
Measurement IFNγ+CD8+ T-cells (flow cytometry)
Smg6wt
Smg6mut
g
sequence
gene/transcript
transcript type
rank %
Peptide intensity (log10)
canonical
common
AAIQGAVAM Ube2o-201 protein coding 0.034
FGIHNGVETL Gpcpd1-205 protein coding 0.015
SNYQHITNF Ap3d1-201 protein coding 0.001
VAPHPVTVPT Fam168b-203 protein coding 9.759
Smg6mut specific
GNVTNITTV Nrros-201 protein coding 0.006
GSYSYTQV Smox-207 protein coding 0.004
NSVQNQIEA Gvin2-202 protein coding 0.015
SAPTNVHASEI Myom3-201 protein coding 0.001
non-canonical
Smg6mut specific
SAPDGIKTPM D17H6S56E-5 viral envelope-like protein 1.045
VVITFSKM Gm6545 processed pseudogene 0.004
VSTTNFTHA Hjv alternative frame 0.018
AGPSNSEIHL Trf intronic region 0.001
h
spleen
liver
IFNγ+CD8+ T-cells (%)
Smg6wt/wt
Smg6mut/mut
P = 0.002
P = 0.003
P = 0.001
P = 0.004
P = 0.06
P = 0.06
P = 0.08
P = 0.02
peptide pool:
- com can non-can
Smg6mut specific

Figure 3. Multiomics-based identifcation and validation of SMG6-dependent immunopeptides

(a) Schematic of the multiomics approach used to identify SMG6-dependent immunopeptide candidates by combining RNA-seq, Ribosome profiling (Ribo-seq) and immunopeptidomics data.

(b) MHC-I binder peptide count and distribution across *Smg6*$^{wt/wt}$ and *Smg6*$^{mut/mut}$ liver replicates (n = 3 mice per genotype). Enrichment of unique peptides in *Smg6*$^{mut/mut}$ samples (18 in all replicates, orange circle) as compared to *Smg6*$^{wt/wt}$ (4 in all replicates, blue circle) is highly significant (P = 0.000053; Fisher's exact test). The heatmap scale is colored according to peptide count, for better visual representation.

(c) Scatter plots of peptide intensity values, showing peptide categories canonical (protein-coding), non-canonical (exonic) and non-canonical (intronic), in *Smg6*$^{wt/wt}$ (x-axis) vs, *Smg6*$^{mut/mut}$ (y-axis). Data are plotted as medians from the three replicates. Unique peptides for one of the genotypes that are found in all three replicates are colored orange (*Smg6*$^{mut/mut}$ -specific peptides) and blue (*Smg6*$^{wt/wt}$-specific peptides), with specific peptides that are used in the downstream pools highlighted and annotated with their amino acid sequence.

(d) RNA-seq (top panels) and Ribo-seq (bottom panels) read pileup plots show the strongly increased transcript and footprint abundance of *D17H6S56E-5* in *Smg6*$^{mut/mut}$. Left panel shows the larger genomic region, including the CDS (highlighted in turquoise) from which the non-canonical polypeptide is translated, while the right panel zooms into the specific region where the immunopeptide is translated (highlighted in light magenta). Plots were generated using merged sequencing data from the three biological replicates (individual livers) per group. Please note gene orientation from right to left.

(e) Normalized exonic and intronic RNA-seq read counts of *D17H6S56E-5*. Each dot represents the merged sequencing data from three biological replicates/livers.

(f) Schematic of the immunogenicity quantification experiment. *Smg6*$^{wt/wt}$ and *Smg6*$^{mut/mut}$ mice were sacrificed 3 weeks post-tamoxifen. Spleens and livers were extracted from the animals and leukocytes were isolated. The cells were then incubated with peptide pools indicated in (g), for 6 hours. The percentages of IFNγ^{+}CD8^{+} T-cells were used as a readout for the immunogenicity of each peptide pool. Common peptides were used as negative control (*Smg6*$^{wt/wt}$, n = 3 mice, *Smg6*$^{mut/mut}$, n = 4 mice).

(g) Table showing peptide sequences derived from the indicated genes, transcript types, rank percentages from NetMHCpan prediction and their intensity in each of three

replicates of *Smg6*$^{wt/wt}$ and *Smg6*$^{mut/mut}$ livers. Each group of four peptides was used as a pool in the experiment in (h).

(h) Overall IFNγ^{+}CD8^{+} T-cell percentage per tissue (left panel, spleen; right panel, liver), as assessed by flow cytometry, upon treatment with no peptide pool (-), canonical common peptide pool (com), canonical *Smg6*^{mut}-specific peptide pool (can), and non-canonical *Smg6*^{mut}-specific peptide pool (non-can). Bars indicate means, and the error bars SEM; individual datapoints are measurements from independent animals (*Smg6*$^{wt/wt}$, n = 3 mice, *Smg6*$^{mut/mut}$, n = 4 mice). The *P*-values were calculated with two-tailed unpaired *t*-test.

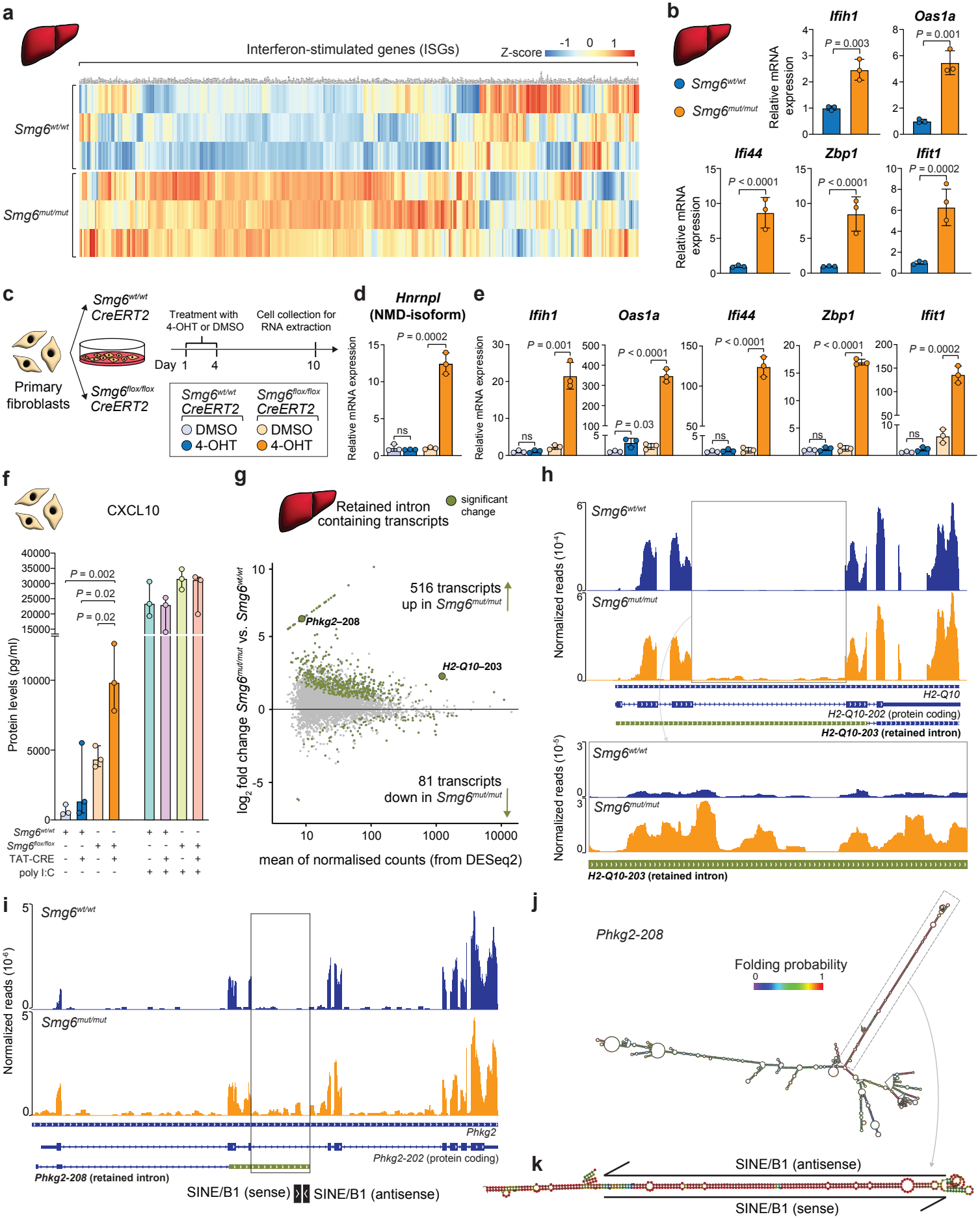
a
Interferon-stimulated genes (ISGs)
Z-score
-1 0 1
Smg6wt/wt
Smg6mut/mut
b
Smg6wt/wt
Smg6mut/mut
Relative mRNA expression
Ifih1
P = 0.003
Oas1a
P = 0.001
Ifi44
P < 0.0001
Zbp1
P < 0.0001
Ifit1
P = 0.0002
c
Primary fibroblasts
Smg6wt/wt CreERT2
Smg6flox/flox CreERT2
Treatment with 4-OHT or DMSO
Cell collection for RNA extraction
Day 1 4 10
Smg6wt/wt CreERT2
Smg6flox/flox CreERT2
DMSO
4-OHT
d
Hnrnpl (NMD-isoform)
P = 0.0002
ns
e
Ifih1
Oas1a
Ifi44
Zbp1
Ifit1
P = 0.001
P < 0.0001
P = 0.03
f
CXCL10
Protein levels (pg/ml)
P = 0.002
P = 0.02
P = 0.02
Smg6wt/wt
Smg6flox/flox
TAT-CRE
poly I:C
g
Retained intron containing transcripts
significant change
516 transcripts up in Smg6mut/mut
81 transcripts down in Smg6mut/mut
Phkg2–208
H2-Q10–203
log2 fold change Smg6mut/mut vs. Smg6wt/wt
mean of normalised counts (from DESeq2)
h
Smg6wt/wt
Smg6mut/mut
Normalized reads (10-4)
Normalized reads (10-5)
H2-Q10
H2-Q10-202 (protein coding)
H2-Q10-203 (retained intron)
i
Smg6wt/wt
Smg6mut/mut
Normalized reads (10-6)
Phkg2
Phkg2-202 (protein coding)
Phkg2-208 (retained intron)
SINE/B1 (sense)
SINE/B1 (antisense)
j
Phkg2-208
Folding probability
0 1
k
SINE/B1 (antisense)
SINE/B1 (sense)

Figure 4. *Smg6* mutation elicits type I IFN response and increased intron abundance

(a) Heatmap showing ISG expression in control and mutant livers (n = 3 livers per group). RNA-seq data was plotted after Z-score transformation of normalized expression levels across the 6 samples.

(b) Relative hepatic mRNA levels of indicated ISGs (n = 3 mice for each group), detected via qPCR. *Smg6*$^{wt/wt}$ (control) samples were set to 1.

(c) Schematic of the experiment to analyze SMG6-dependent ISG expression. To induce *Smg6* mutation in *Smg6*$^{flox/flox}$; *CreERT2* fibroblasts, cells were treated with 2 μM 4-hydroxytamoxifen (4-OHT) during days 1 to 4, and cells were collected 6 days later (day 10) for RNA isolation and qPCR. Control treatment was DMSO.

(d) Relative mRNA expression of the endogenous, diagnostic NMD-target, an *Hnrnpl* splice form, in samples collected as described in (c). Three biological replicates were used per group.

(e) Relative mRNA expression of indicated ISGs in same samples as in (d). Three biological replicates were used per group.

(f) Analysis of CXCL10. At day 1, *Smg6*$^{wt/wt}$ and *Smg6*$^{flox/flox}$ cells were treated with TAT-CRE (2.5 μM, 8 hours) or vehicle. At day 7, indicated groups were treated with poly I:C to serve as positive control (1 μM, 8 hours). At day 10, supernatants were collected, and CXCL10 levels were detected via ELISA. Data are plotted as medians (n = 3 biological replicates for each group). The *P*-values were calculated with two-tailed unpaired *t*-test.

(g) Differential expression analysis at the transcript level, specifically on retained intron containing mRNAs, comparing *Smg6*$^{wt/wt}$ and *Smg6*$^{mut/mut}$ livers (n = 3 mice per genotype). Significantly more or less abundant transcripts are indicated in olive, showing strong skew to upregulation. Two transcripts are individually labeled, as they are further shown in panels (h) and (i)

(h) RNA-seq pileup plots show the upregulated transcript isoform (containing intron) for *H2-Q10*. Top panels show the larger genomic region, including the retained intron, while bottom panels zoom in the retained intron area. Plots were generated using merged sequencing data from three biological replicates per group. Please note gene orientation from left to right.

(i) RNA-seq pileup plots as in (h) show the increased abundance of the intron-containing transcript isoform for *Phkg2.* Genomic area where SINE/B1 elements are located in intronic region is highlighted. Plots were generated using merged sequencing data from three biological replicates per group. Please note gene orientation from left to right.

(j) RNA structure prediction of *Phkg2-208* by RNAfold web server, showing extensive predicted dsRNA region.

(k) Predicted double-stranded structure from SINE/B1 elements located in the intronic region of *Phkg2-208* transcript.

For (b), (d) and (e) data are plotted as means, and the error bars indicate SEM. The *P*-values were calculated with two-tailed unpaired *t*-test.

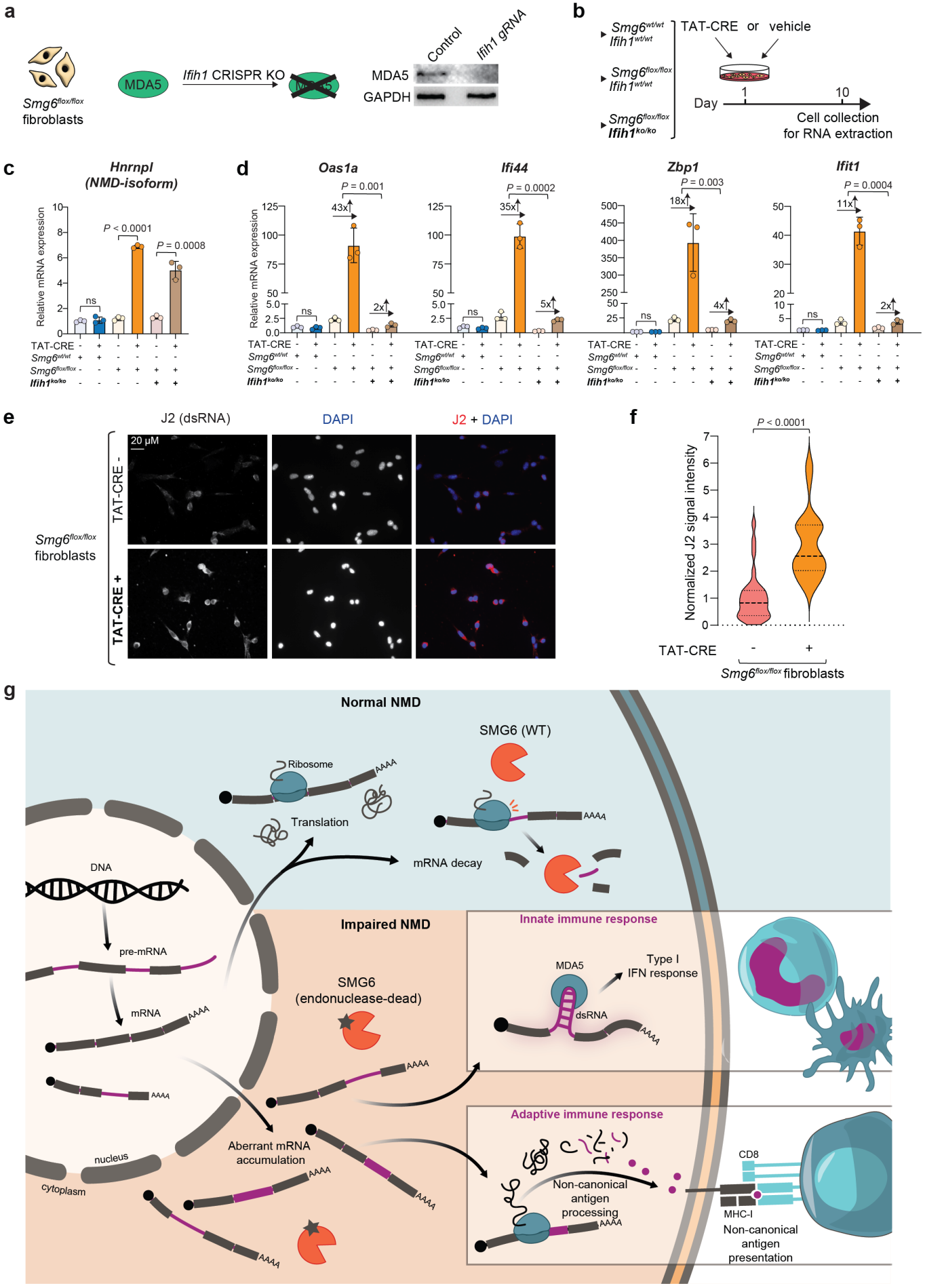
a
Smg6flox/flox fibroblasts
MDA5
Ifih1 CRISPR KO
Control
Ifih1 gRNA
MDA5
GAPDH
b
Smg6wt/wt Ifih1wt/wt
Smg6flox/flox Ifih1wt/wt
Smg6flox/flox Ifih1ko/ko
TAT-CRE or vehicle
Day
1
10
Cell collection for RNA extraction
c
Hnrnpl (NMD-isoform)
Relative mRNA expression
P < 0.0001
P = 0.0008
ns
TAT-CRE
Smg6wt/wt
Smg6flox/flox
Ifih1ko/ko
d
Oas1a
Ifi44
Zbp1
Ifit1
P = 0.001
P = 0.0002
P = 0.003
P = 0.0004
43x
35x
18x
11x
2x
5x
4x
2x
ns
e
J2 (dsRNA)
DAPI
J2 + DAPI
20 µM
TAT-CRE -
TAT-CRE +
Smg6flox/flox fibroblasts
f
P < 0.0001
Normalized J2 signal intensity
TAT-CRE
-
+
Smg6flox/flox fibroblasts
g
Normal NMD
SMG6 (WT)
Ribosome
AAAA
Translation
mRNA decay
DNA
pre-mRNA
mRNA
Impaired NMD
SMG6 (endonuclease-dead)
Innate immune response
MDA5
Type I IFN response
dsRNA
Adaptive immune response
Aberrant mRNA accumulation
nucleus
cytoplasm
Non-canonical antigen processing
CD8
MHC-I
Non-canonical antigen presentation

Figure 5. *Smg6* mutation drives type I IFN response through dsRNA sensor MDA5

(a) Western blot validation of the loss of MDA5 expression in *Ifih1*$^{ko/ko}$ fibroblasts (in background of *Smg6*$^{flox/flox}$ fibroblasts). GAPDH serves as loading control.

(b) Schematic of the experiment. Cells with indicated genotypes were treated with either TAT-CRE (2.5 μM) or vehicle for 8 hours, and then harvested at day 10 for RNA extraction and qPCR analyses.

(c) Relative mRNA expression of the endogenous, diagnostic NMD-target, an *Hnrnpl* splice form, in samples collected as described in (b). Three biological replicates were used per group.

(d) Relative mRNA expression of indicated ISGs. Arrows indicate the fold-change in the expression of indicated genes between cells nontreated vs. treated with TAT-CRE. Three biological replicates were used per group.

(e) Representative immunofluorescence images using dsRNA-specific antibody J2 (red) on *Smg6*$^{flox/flox}$ fibroblasts that were not treated (top) or treated (bottom) with cell-permeable TAT-CRE to induce *Smg6* mutation. DAPI (blue) serves to visualize nuclei.

(f) Quantification of J2 signal intensity (n = 238 cells for TAT-CRE-negative, n = 185 cells for TAT-CRE-positive). Median and third quartiles of each group are marked by dotted lines. The *P*-value was calculated with two-tailed unpaired *t*-test.

(g) Model for how the suppression of NMD activity via endonuclease-inactive SMG6 activates both innate and adaptive branches of the immune system. For innate responses, aberrant mRNAs (shown here: intron-retained transcripts known to contain repetitive elements) can form double-stranded configurations, causing activation of cytoplasmic dsRNA sensor MDA5, which upregulates a type I IFN response, resulting in innate immune cell infiltration. With the accumulation of aberrant or otherwise NMD-suppressed mRNAs in the cytoplasm, their translation leads to the production of unusual/non-canonical peptides which are then subsequently processed for MHC-I presentation on the cell surface, which attracts CD8^{+} T-cells to infiltrate the tissue, leading to adaptive immune cell recognition. Please note that for simplicity, prior steps required for CD8^{+} T-cell activation (i.e., antigen presentation by dendritic cells) have been omitted from the schematic.

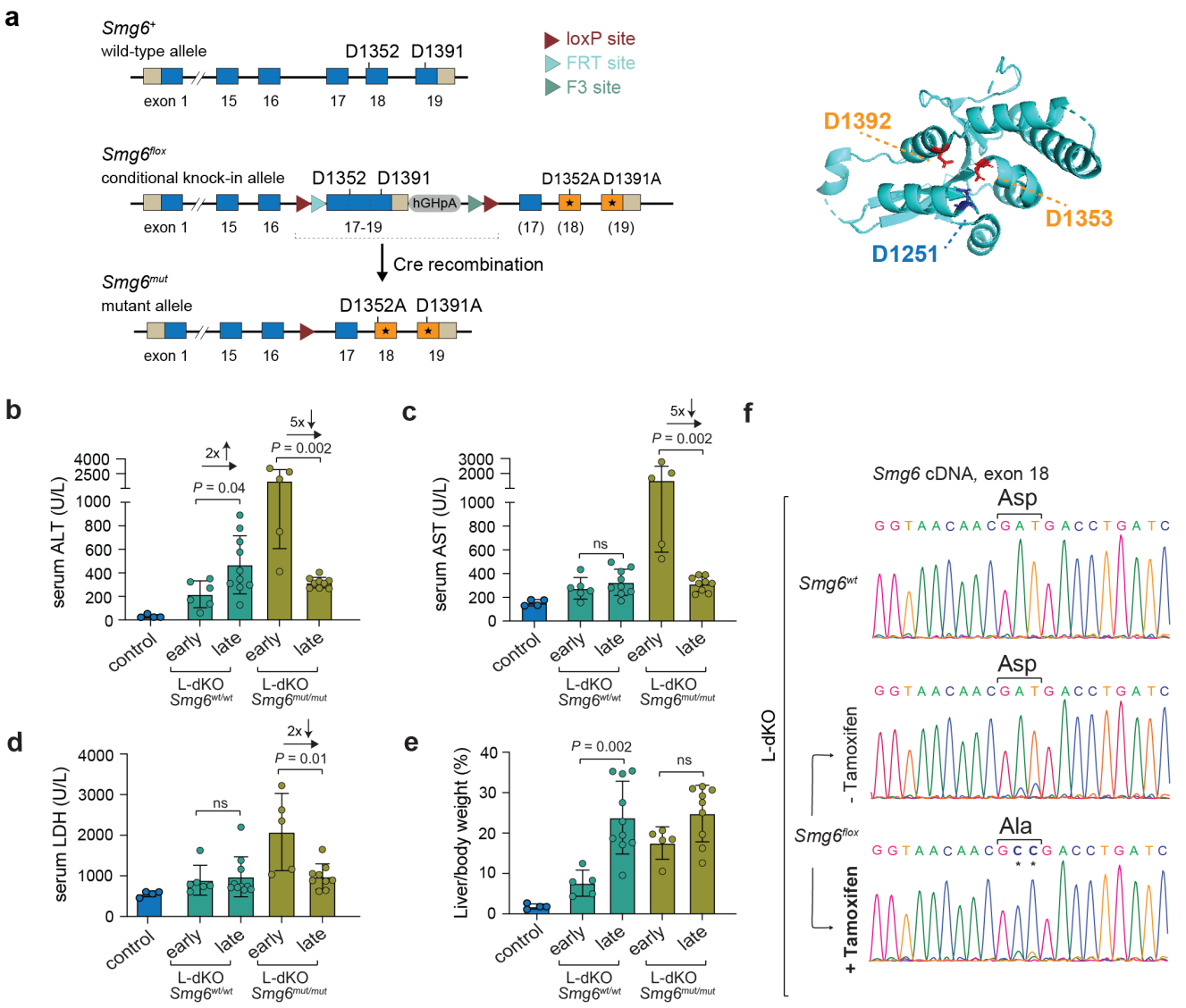

Extended Data Figure 1. Regression of liver damage marker levels in *Smg6* mutant mice from early- to late-stage L-dKO.

(a) Schematic of the genetic NMD-deficient mouse allele based on *Smg6*. *Smg6*^{flox} expresses wild-type SMG6 protein encoded by the blue exons; after Cre-mediated recombination to *Smg6*^{mut}, point-mutated exons 18 and 19 (orange) lead to the expression of mutant SMG6 (D1352A, 1391A). The right panel shows the structure of the human protein (PDB accession 2HWW) with the corresponding mutated aspartic acid residues (in orange) that are within the catalytic triade of the PIN nuclease domain. Please note that human Asp1392 corresponds to mouse Asp1391, and human Asp1353 to mouse Asp1352. Figure adapted from [16].

(b-d) Comparison of the levels of indicated liver damage enzymes, detected in serum, between early- and late-stage mice. Arrows display the fold-change alteration in the

level of liver damage markers from early- to late-stage, in the same group (n = 4 mice for control, n = 5 mice for early-stage groups; L-dKO *Smg6*^{wt} late, n = 10 mice; L-dKO *Smg6*^{mut} late, n = 9 mice).

(e) Comparison of the ratio of liver-over-body weight between early- and late-stage mice, within the same group (n = 5 mice for early-stage groups; L-dKO *Smg6*^{wt} late, n = 10 mice; L-dKO *Smg6*^{mut} late, n = 9 mice).

(f) Sanger sequencing chromatograms on cDNA, from representative late-stage livers, show the conversion of aspartic acid (Asp) encoding wild-type codon (GAT) to alanine (Ala) encoding mutant codon (GCC), at the position in exon 18 that codes for one of the Asp residues of the catalytic center of SMG6 that was targeted in the genetic model, through tamoxifen-induced CreERT2 activation in liver.

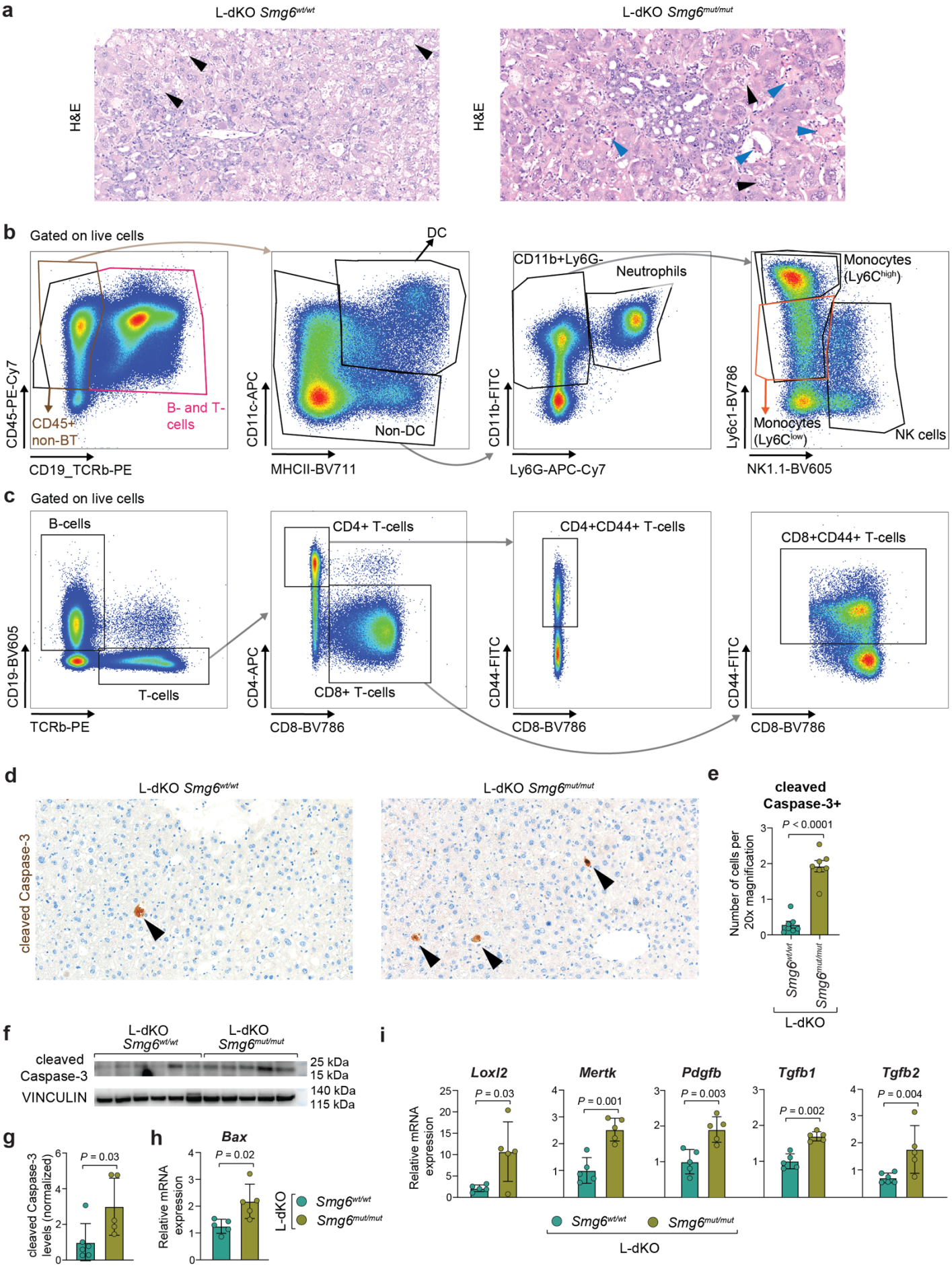
a
L-dKO Smg6wt/wt
L-dKO Smg6mut/mut
H&E
H&E
b
Gated on live cells
CD45+ non-BT
B- and T-cells
CD45-PE-Cy7
CD19_TCRb-PE
DC
Non-DC
CD11c-APC
MHCII-BV711
CD11b+Ly6G-
Neutrophils
CD11b-FITC
Ly6G-APC-Cy7
Monocytes (Ly6Chigh)
Monocytes (Ly6Clow)
NK cells
Ly6c1-BV786
NK1.1-BV605
c
Gated on live cells
B-cells
T-cells
CD19-BV605
TCRb-PE
CD4+ T-cells
CD8+ T-cells
CD4-APC
CD8-BV786
CD4+CD44+ T-cells
CD44-FITC
CD8-BV786
CD8+CD44+ T-cells
CD44-FITC
CD8-BV786
d
L-dKO Smg6wt/wt
L-dKO Smg6mut/mut
cleaved Caspase-3
e
cleaved Caspase-3+
P < 0.0001
Number of cells per 20x magnification
Smg6wt/wt
Smg6mut/mut
L-dKO
f
L-dKO Smg6wt/wt
L-dKO Smg6mut/mut
cleaved Caspase-3
VINCULIN
25 kDa
15 kDa
140 kDa
115 kDa
g
cleaved Caspase-3 levels (normalized)
P = 0.03
h
Bax
P = 0.02
Relative mRNA expression
L-dKO
Smg6wt/wt
Smg6mut/mut
i
Loxl2
P = 0.03
Mertk
P = 0.001
Pdgfb
P = 0.003
Tgfb1
P = 0.002
Tgfb2
P = 0.004
Relative mRNA expression
Smg6wt/wt
Smg6mut/mut
L-dKO

Extended Data Figure 2. Cellular changes following *Smg6* mutation in liver.

(a) Representative H&E images from early-stage L-dKO livers, at 20x magnification. Black arrowheads indicate hepatocyte ballooning in both livers, while blue arrowheads mark apoptotic hepatocytes in L-dKO *Smg6*^{mut} tissue.

(b) Flow cytometry gating strategy of intrahepatic myeloid cells.

(c) Flow cytometry gating strategy of intrahepatic lymphocytes.

(d) Representative IHC images of livers from early-stage mice, stained with antibodies directed against cleaved Caspase-3, at 20x magnification. Arrowheads show cleaved Caspase-3+ cells (brown).

(e) Quantification of cleaved Caspase-3 IHC images as that shown in (d). For each sample, the number of cleaved Caspase-3+ cells was counted in 10 randomly selected images, at 20x magnification (mean values from 7 mice per group).

(f) Western blot analysis of total proteins, for cleaved Caspase-3. VINCULIN served as loading control (L-dKO *Smg6*^{wt}, n = 6 mice; L-dKO *Smg6*^{mut}, n = 5 mice).

(g) Quantification of Western blot from (f).

(h) Relative hepatic mRNA levels of *Bax*, from early-stage mice (n = 5 mice per group).

(i) Relative hepatic mRNA levels of indicated pro-fibrotic genes, from early-stage mice (n = 4 mice per group).

For (e), (g), (h), and (i) data are plotted as means, and the error bars indicate SEM. The *P*-values were calculated with two-tailed unpaired *t*-test.

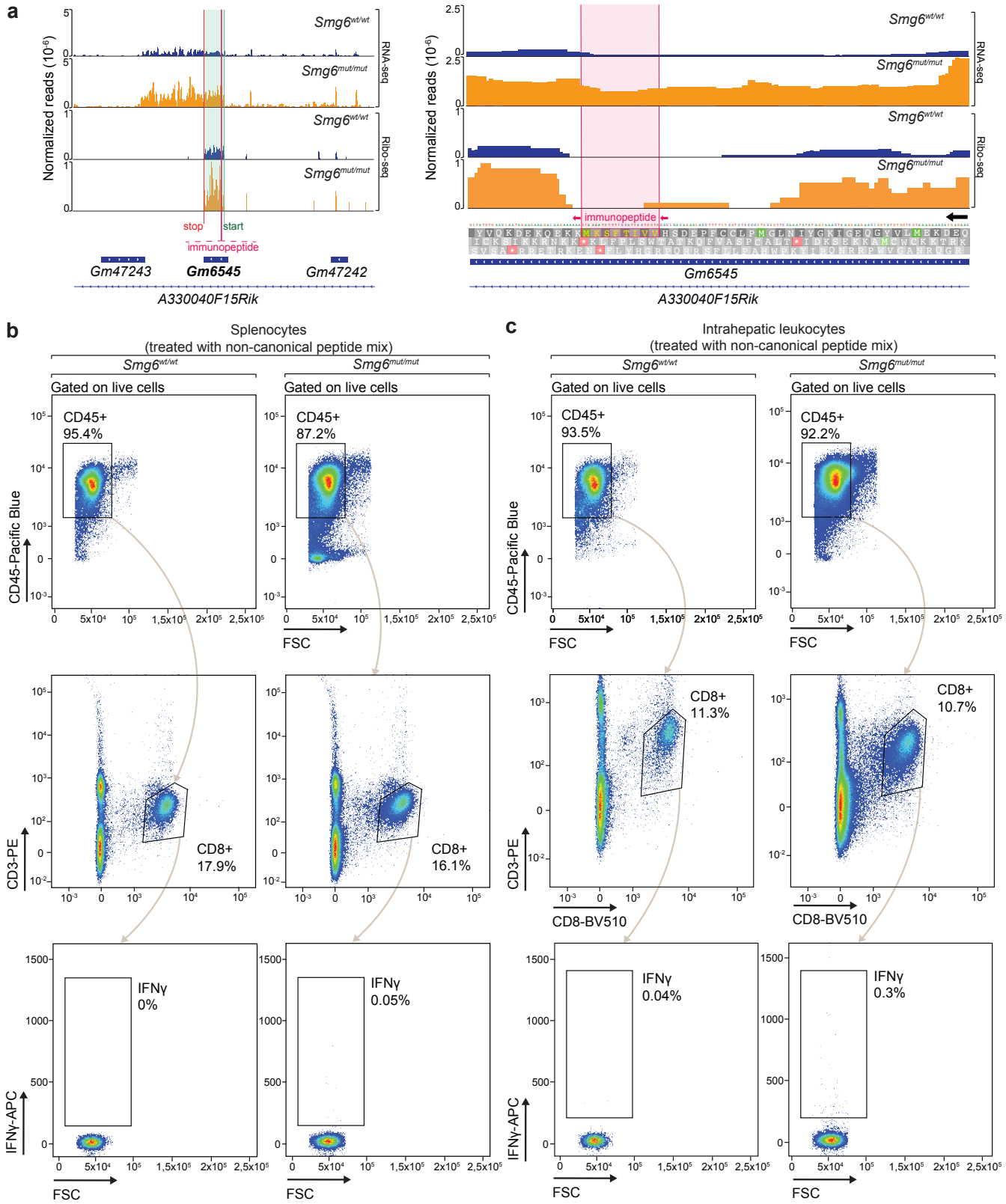
a
Normalized reads (10⁻⁶)
Smg6wt/wt
Smg6mut/mut
RNA-seq
Ribo-seq
stop
start
immunopeptide
Gm47243
Gm6545
Gm47242
A330040F15Rik
immunopeptide
Gm6545
A330040F15Rik
b
Splenocytes
(treated with non-canonical peptide mix)
Smg6wt/wt
Smg6mut/mut
Gated on live cells
CD45+
95.4%
CD45+
87.2%
CD45-Pacific Blue
FSC
CD8+
17.9%
CD8+
16.1%
CD3-PE
IFNγ
0%
IFNγ
0.05%
IFNγ-APC
c
Intrahepatic leukocytes
(treated with non-canonical peptide mix)
CD45+
93.5%
CD45+
92.2%
CD8+
11.3%
CD8+
10.7%
CD8-BV510
IFNγ
0.04%
IFNγ
0.3%

Extended Data Figure 3. Increased non-canonical antigen expression in *Smg6* mutant livers.

(a) RNA-seq (top panels) and Ribo-seq (bottom panels) read coverage plots show upregulated transcript and ribosome footprint abundance for *Gm6545* in *Smg6*$^{mut/mut}$ compared to *Smg6*$^{wt/wt}$. Left panel shows the whole genomic region, including the CDS (highlighted in turquoise) where the non-canonical polypeptide is translated, while right panel zooms into the specific region where the immunopeptide is translated (highlighted in light magenta). Read coverage plots were generated by merging sequencing data from three biological replicates (individual livers) per group.

(b, c) Representative flow cytometry gating strategies for one liver and one spleen from each group for IFNγ^{+}CD8^{+} T-cells, treated with non-canonical peptide pool.

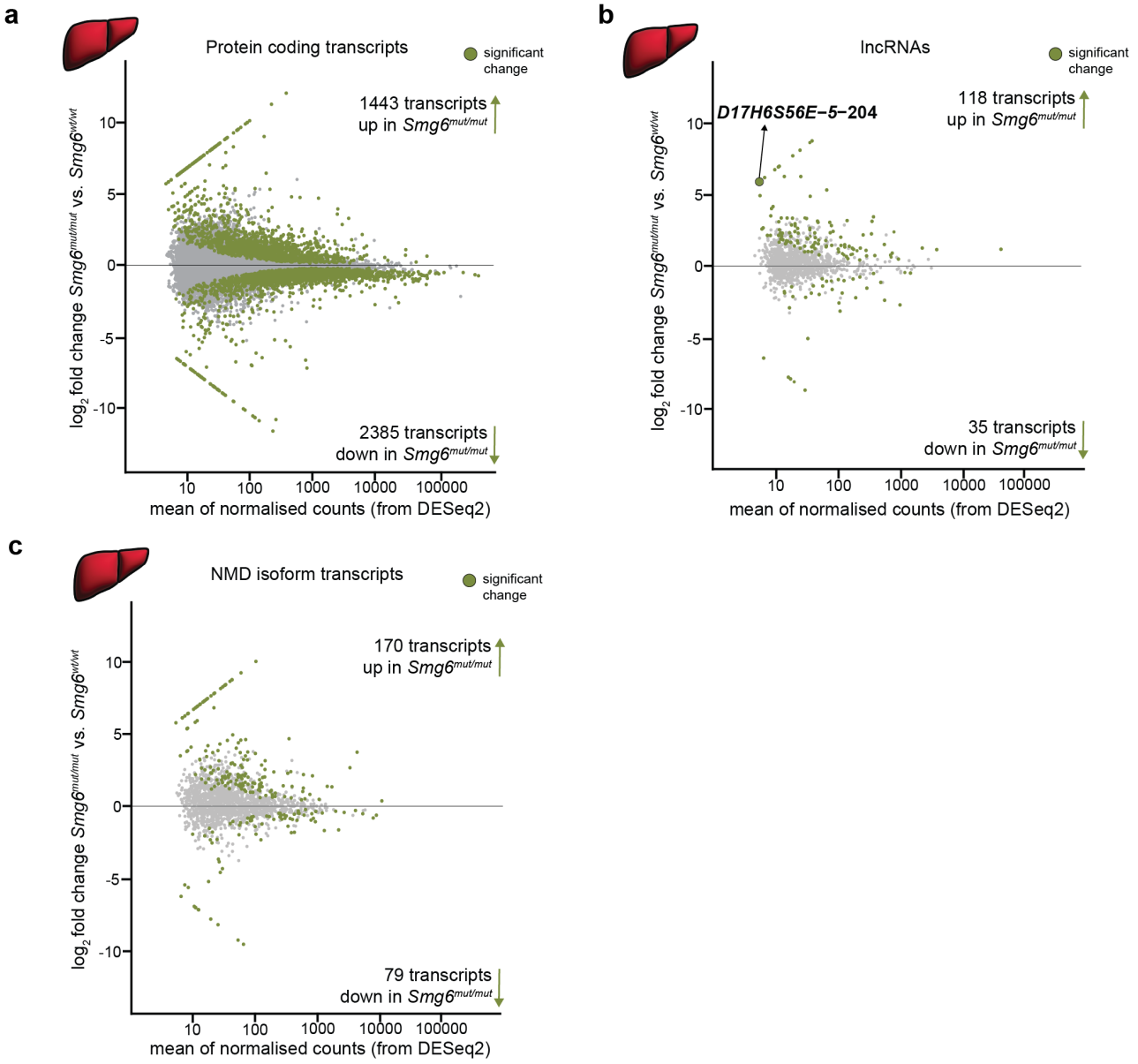

Extended Data Figure 4. RNA-seq analysis from *Smg6*^{mut} vs. *Smg6*^{wt} livers for different transcript biotypes.

(a-c) Differential expression analysis of liver transcriptomics data for protein coding transcripts (a), lncRNAs (b), and annotated NMD isoform transcripts (c). Significantly changed transcripts are highlighted in olive.

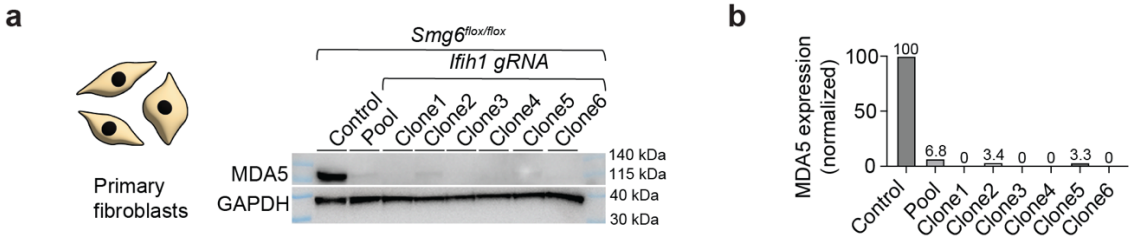

Extended Data Figure 5. Deletion of *Ifih1* in *Smg6*$^{flox/flox}$ fibroblasts via CRISPR.

(a) Western blot confirmation of the loss of MDA5 activity in different fibroblast single-cell clones. GAPDH serves as loading control.

(b) Quantification of Western blot from (a).